Contents

Sommario

Questa tesi riguarda l'analisi automatica di immagini del fundus oculare e le sue applicazioni alla diagnotica oftalmologica.

Il diabete è una malattia che si sta diffondendo sempre di più nel mondo, a causa dell'aumento demografico, dell'età, dell'urbanizzazione e per l'inattività fisica che porta all'obesità, per cui la retinopatia diabetica è fra le cause principali di cecità.

Anche l'ipertensione colpisce la microcircolazione e la retinopatia ipertensiva è una conseguenza di questo danno.

In questa tesi saranno presentati dei nuovi algoritmi di elaborazione ed analisi automatica di immagini della retina che possono aiutare la diagnosi e che possono essere utilizzati in sistemi automatici di screening della retinopatia diabetica.

E' stato sviluppato un algoritmo veloce e robusto per la registrazione di immagini, per ottenere una immagine completa da una squenza di viste parziali, con una percentuale di fallimento di solo il 2% su immagini acquisite con una fundus camera Nidek Orion.

Successivamente saranno presentati dei metodi per discriminare i falsi positivi dai veri positivi in algoritmi per la segmentazione dei vasi sanguigni basati su tecniche di tracking.

L'individuazione della posizione del disco ottico è un prerequisito per il calcolo di un importante indice di retinopatia, il rapporto dei diametri arteria\vena, per cui viene proposto un nuovo metodo per raffinare la localizzazione del disco ottico e individuare il bordo usando un active contour model, ottenendo un errore medio di 3.4 pixel nell'individuazione del bordo (su immagini di dimensione 1392x1038).

L'identificazione della fovea è un compito fondamentale in ogni studio di malattie oculari, poiché è la zona di maggiore acutezza visiva dela retina, quindi le lesioni vicine alla fovea sono più gravi.

E’ stato quindi sviluppato un nuovo algoritmo per l’identificazione della fovea, con una distanza media di 35 pixels (su immagini 1700x1700) dalla posizione della fovea segnata a mano da un oftalmologo.

Summary

This thesis deals with the automatic analysis of color fundus images and with its application to diagnostic ophthalmology.

Diabetes is a growing epidemia in the world, due to population growth, aging, urbanization and increasing prevalence of obesity and physical inactivity, so diabetic retinopathy has an ever increasing importance as a cause of blindness. Also hypertension affects the microcirculation and hypertensive retinopathy is one of the consequences of such damage.

In this thesis new algorithms to help ophthalmologist's diagnosis and to be used in automated systems for retinopathy screening will be presented .

We have developed a fast and robust algorithm for retinal image registration, to build a mosaic image from a sequence of partial views, with a failure rate of only 2% on images acquired with an automatic fundus camera Nidek Orion. Then methods to discriminate false detections from true positives in algorithms for blood vessels extraction based on tracking techniques will be presented, with a sensitivity of 63% and accuracy of 95%.

The detection of optic disc position is also a prerequisite for the computation of an important diagnostic index for hypertensive/sclerotic retinopathy based on vasculature, the arteriolar-to venular diameter ratio, so a new method to refine the localization of the optic disc and to detect its border using an active contour model is proposed, with an average error of 3.4 pixels on border detection(on 45° images with size 1392x1038 pixels) .

Fovea identification is a fundamental task in any study of ocular diseases, because it's the most accuracy vision zone of the retina, so the nearer the fovea are the graver the ocular lesions are. Therefore we have developed a new algorithm for the automatic identification of the fovea, with an average distance from the manual labelled fovea position of 35 pixels (on 45° mosaic images with size 1700x1700 pixels)

Chapter 1

Introduction

Hypertensive retinopathy is associated with systemic arterial hypertension; retinal vascular changes that may occur are seen in both chronic and acute stages. It is likely that increasingly more patients will present hypertension, which is ranked as one of the top 10 risk factors for burden of diseases in developed countries by the World Health Organization. Ophthalmologists are in a unique position to detect the disease, as well as prevent visual loss from it; a patient with undiagnosed malignant hypertension will probably consult first an ophthalmologist with a complaint of visual loss, that is ultimately related to hypertension.

An even more dramatic situation characterizes diabetes related retinopathy.

Diabetes is a growing epidemia in the world, due to population growth, aging, urbanization and increasing prevalence of obesity and physical inactivity: population with diabetes is estimated to grow by the 37 percent by 2030, and today it is already around 200 millions people worldwide. Following the trend of diabetes, diabetic retinopathy has an ever increasing importance as a cause of blindness: in the United States it is the first cause of blindness in people in working age, with all the consequent economic and social burdens. The timely diagnosis and referral for menagement of diabetic retinopathy can prevent 98% of visual loss. It is estimated that the underlying cause of blindness in the majority of diabetic patients is not diabetic retinopathy per se but the misdiagnosis of diabetic retinopathy.

Currently, a periodic dilated direct ophthalmoscopic examination seems the best approach for a screening with near universal coverage of the populationat risk, despite the proved low sensitivity of direct ophthalmoscopy. However, the number of ophthalmologist available is the limiting factor in initiating an ophthalmologist based screening. With the

increasing availability of digital fundus camera, the automatic analysis of such digital images might allow to develop an inexpensive screening device that could be used without the need for medical assistance.
Moreover computer vision techniques applied to retinal image analysis proved of great help to ophthalmologists, allowing the rapid and reliable extraction of important diagnostic indexes.

1.1 – Aim and Objectives

The aim of the work presented in this thesis is to develop a set of new algorithms to help ophthalmologist's diagnosis and to be used in automated systems for retinopathy screening.
At first, we have faced the task of building a mosaic image from a sequence of partial views acquired with an automatic fundus camera Orion Nidek , which takes five images representing different fields of the retina.
An image registration technique is proposed to solve this problem. This algorithm is fast and robust (2% of failure rate) and can be used in order to obtain a complete, non-redundant view of the retina combining several different fields of view, and also to quantitatively compare images taken at different examinations for monitoring the progression of the disease.
Then we will present new methods for the detection of the main anatomical structures of the retina(retinal vessel network, optic disc, fovea). This is an essential task for any system of analysis of fundus images because it allows the classification of lesions and the extraction of important diagnostic parameters.
Automatic extraction of the retinal vessel network is important because retinal vessels are very sensitive to changes in the microvascular circulation, so an early warning about serious cardiovascular diseases can be provided by the analysis of microvasculature health status. A previously developed algorithm for vessel extraction based on a tracking technique has been improved adding a module that discriminate false detections from true positives.

On retinal images, a sign that have been shown to be related to cardiovascular diseases is the generalized arteriolar narrowing, usually expressed by the arteriolar-to venular diameter ratio (AVR) [34-35]. In this thesis a system for AVR estimation that is completely automatic, avoiding long and cumbersome manual measurements, will be proposed.

The extraction of the retinal vessel network is a prerequisite also for the recognition of the optic disc, and for the elimination of the vascular structures from the search of possible non-vascular lesions. Locating the OD position is important to exclude it from the set of possible lesions, to compute AVR and to establish a frame of reference within the retinal image. Disc boundary detection is also important to assess the progression of glaucoma, which is due to an increase in intra-ocular pressure and produces additional pathological cupping of the optic disc.

Fovea identification is a fundamental task in any study of ocular diseases, because it's the most accuracy vision zone of the retina, so the nearer the fovea are the graver the ocular lesions are.

1.2 – Outline of the Thesis

Chap. 2-4 are introductory chapters describing retinal imaging, image acquisition protocols and the experimental setting of this thesis. The fundus camera examination, the appearance of the retina in a fundus image and the main findings of hypertensive and diabetic retinopathy will be described in Chap. 2.

In Chap. 3 the available imaging protocols for retinopathy evaluation will be reviewed.

In Chap. 4 will be presented protocols and instruments used to acquire the images on which we have tested the algorithms.

The image registration and mosaicing algorithm will be described in Chap. 5.

The procedure to discriminate false detections from true positives in tracking-based blood vessel automatic extraction is the object of Chap. 6, and the identification of the optic disc of Chap.7

The algorithm for the automatic identification of the fovea is described in Chap.8, and in Chap. 9 is presented a new method for automatic estimation of the arteriolar-to venular diameter ratio.

Chapter 2

Fundus Images and its Diagnostic Signs

In this chapter a brief review will be presented about what is seen in an image from a fundus camera examination and all the most relevant lesions to be found in the hypertensive and diabetic retinopathy.

2.1 – Fundus Oculi Examination

The first instrument that made available to ophthalmologists the direct examination of the retina was the direct ophthalmoscope, which is still used today. It was first described by Helmholtz at the end of the XIX century, and since then it has not changed much. In its basic form is composed by a light source and a set of lenses. The light is projected through the dilated pupil onto the retina, and the lenses focus on so that the observer can look at the retina. Its use is widespread in the clinical practice, but it has been proved to provide poor sensitivity and results highly dependent on the observer experience.

In the middle of the XX century the first instrument able to acquire photographs of the retina appeared. This is a photographic 35mm back connected to an optic system that focuses on the fundus oculi, illuminated by a coaxial flash. This fundus camera enables the photography of different portions of the retina with different magnification, which ranges from 10^0 to 60^0.

Around 1990, the first digital fundus camera appeared. The optic system is not connected anymore to a traditional camera, but to a CCD, and the image is sent to a computer for visualization and storage.

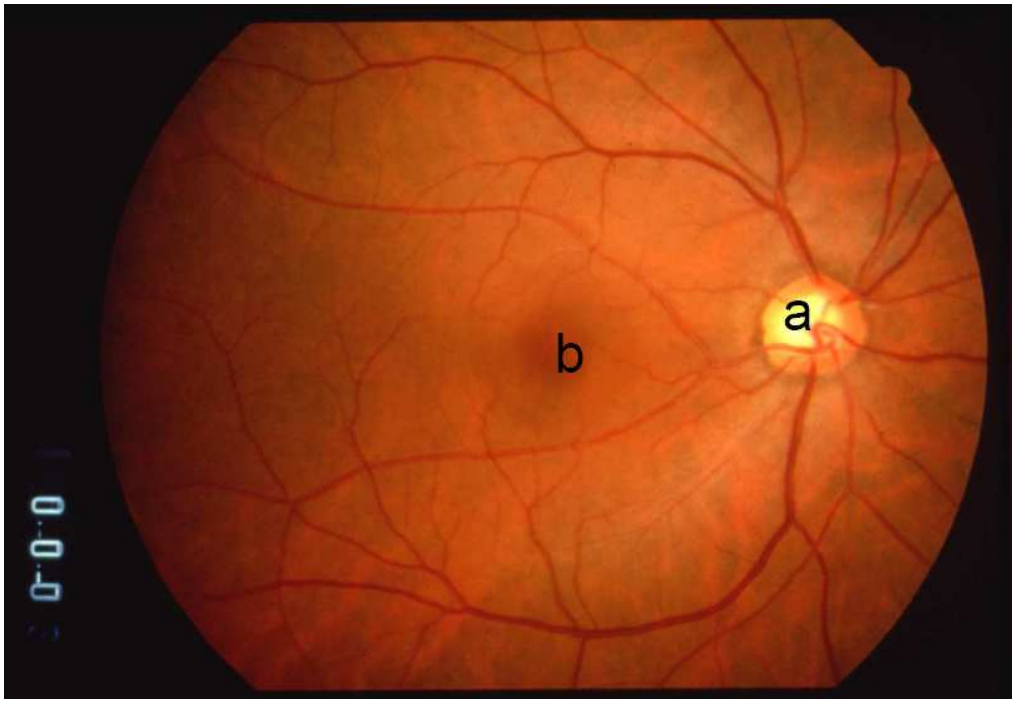

Fig. 2.1: An image of a normal fundus oculi. Papilla (a), fovea (b) and vessel networks are clearly visible

2.1.1 Fundus Oculi Appearance

Using a fundus camera, an image of the fundus oculi is acquired. The visible part of it is composed by the retina with its vascular network and the optic nerve head. The choroid is the structure below the retina and its usually obscured by it.

The retina is a multilayer structure, which is transparent except for the deepest layer, the pigmented epithelium. This gives to the retina its reddish colour. More superficially than the pigmented epithelium there is the sensorial retina, composed by the photoreceptor cells and by the gangliar cells.

The axons of the gangliar cells runs to the papilla, or optic disc, or optic nerve head, which is the place where the bundle of nervous fibers forms the optic nerve, and leaves the optic bulb. From the center of the optic disc the ophthalmic artery enters into the optic bulb, and subsequently branches to provide vascularization to most of the retina. From the capillary network

originates the venous vessels, which flow into the central retinal vein that exit the ocular bulb through the optic disc. Topologically, the temporal vessel arcades delimit the posterior pole. At the center of the posterior pole there is the macula: its center is occupied by a small depression, the fovea, that is the region most densely packed with photoreceptor of the retina and is normally the center of vision. The macula is not fed by retinal vessels, but takes its nutrients from the choroid vessels below the retina.

Choroidal vessels are not usually visible in an image taken with a fundus camera, but if the the pigmented epithelium is very lightly pigmented or in case of pathological depigmentation, the retina becomes almost transparent and the choroid becomes visible.

2.2 – Main Vascular Abnormalities

2.2.1 Tortuosity

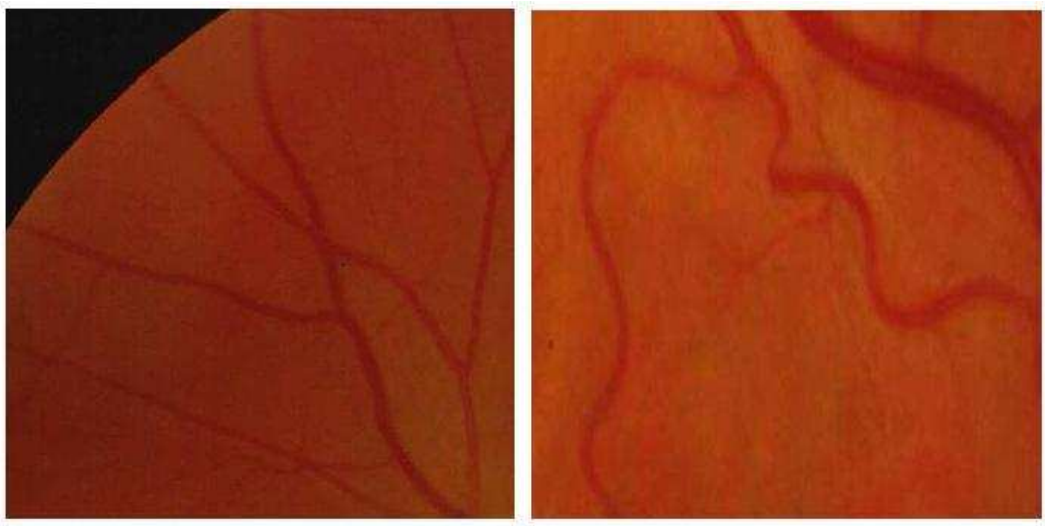

(a) Normal Vessel Course (b) Tortuous Vessels

Figure 2.2: Normal and tortuous vessels

In presence of high blood pressure, vessels may increase in length and vessel walls thicken, and as a result they become increasingly tortuous. This

is at first seen in arteries, and only in more severe stages of retinopathy, also in veins.

2.2.2 Generalized Arterioral Narrowing

The earliest fundus change due to hypertension is the thinning of the retinal arterioles. Narrowing of the arterioles is usually proportional to the degree of elevation of blood pressure. However, retinal arteriolar narrowing is imprecisely quantified from a clinical ophthalmoscopic examination, since the examiner should estimate the normal vessel width prior to the narrowing to evaluate severity of the latter.

2.2.3 Focal Arterioral Narrowing

Figure 2.3: A definite focal narrowing

In severe hypertension states, irregularities in the caliber of blood vessels may appear. In arterioles, they are due to localized spasm and contraction of

the wall. They appear as a focal thinning of the blood column: the narrowing may increase until the vessels become thread-like.

2.2.4 Bifurcations Abnormalities

Arterial diameters and topography at branch points are believed to conform to design principles that optimize circulatory efficiency and maintain constant shear stress across the network [46]. It has been suggested that arterial diameters at a bifurcation should conform to a power relationship, and arterial branches in various circulation have been shown to obey to this design.

It has been shown that bifurcation angles are reduced with increasing hypertension, probably because the atheroma fibrosis of the central artery displace by contraction the arteries toward the disk. Although the mechanisms of bifurcation changes are not clear, both branching angles and also the value ofthe junction exponent seems to deviate from its optimal values with age [47].

2.2.5 Crossing Abnormalities

The abnormal changes in arteriovenous crossings result from the thickening of the wall of the arterioles due to hypertension and sclerosis, and associated changes in the veins at the crossings. The first appearance of crossing abnormalities

is the compression of the vein by the artery, which may vary in severity from a slight indentation to complete interruption of the vein where the artery crosses. When the sclerotic process in the artery extends to the adventitia of the vein, the blood column in the vein will be partially obscured and appear tapered on each side of the crossing.

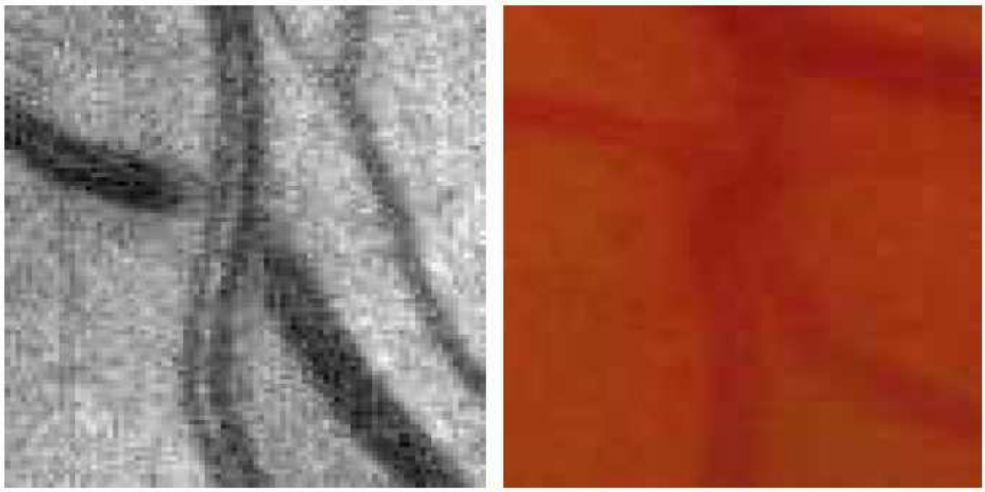

(a) Gunn's sign (Vein compression) (b) Salus's sign (Vein deflection)

Figure 2.4: Gunn's and Salus's sign

Constriction and compression of the veins may impede the blood return, so that the veins become distended for some distance peripheral to the crossing: this is the so called Gunns sign.

The arterial sclerosis may cause deflection of the vein from its normal course at the point where the artery crosses. The vein may deflect both vertically (dipping under the artery or humping over it), or laterally. In this last case, instead of crossing the artery obliquely, the vein does so at right angles and appears as S-shaped at the bend, which has been referred as the Salus sign.

2.3 – Main Non Vascular Findings

2.3.1 Microaneurysms and Red Dots

Retinal microaneurysms are the most characteristic lesion of diabetic retinopathy, but are present also in other pathologies that affect the microvessels. Micoraneurysms are a small dilation of a capillary wall. It is not clear if retinal microaneurysms are due to a vessel wall damage or to the beginning of a neovascolarization. However, the result is the appearance of small saccular structures, of approximate dimension between $10\,\mu m$ and $100\,\mu m$, that in the retinal fluorescein angiography appear as bright hyperfluorescen spots, whereas in colour fundus images appears as round, red spots. They are indistinguishable from small hemorrhages of the same dimension, since they both are small round regions, with a dark red colour. Therefore, both microaneurysms and hemorrhages smaller than the major vein caliber at the optic disc margin (usually 125 ¹m), are considered red dots, and evaluated as microaneurysms [48]. On the contrary, any red spot greater than that is considered an hemorrhage, unless features as round shape, smooth margins and a central light reflex suggest that it is probably a microaneurysm.

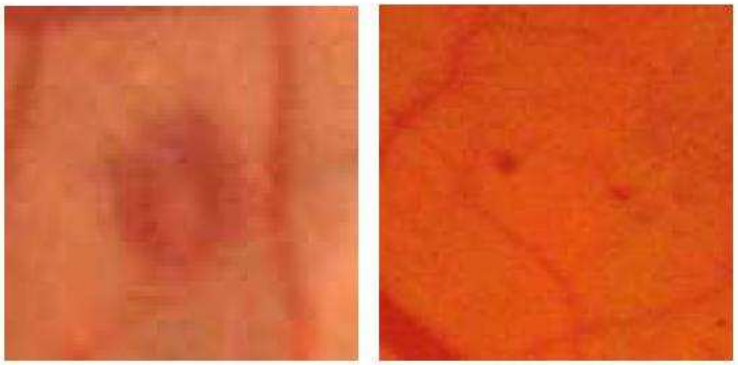

(a) Large microaneurysm with central reflex (b) Microaneurysms

Figure 2.5: Microaneurysms

2.3.2 Hemorrhages

Retinal hemorrhages are blood deposits on the retina. Hemorrhages disappear as the blood is reabsorbed with time.

They are due to the breaking of a vessel wall or of a microaneurysm, and the increase in their presence is a clear sign of diffuse retinal damage.

They have very different shapes, going from the round red spot with sharp margins, to the blot hemorrhage, to the flame-shaped hemorrhage. As the blood is reabsorbed, hemorrhage margins fade and the characteristic red colour turns to a faint greyish-red before disappearing completely.

2.3.3 Hard Exudates

Hard exudates are small lipidic and proteinic deposits, which appear as white or yellowish-white areas with sharp margins. They may be arranged as individual dots, confluent patches or in partial or complete rings surrounding microanaeurysms or zones of retinal edema. In the more severe cases of hypertensive retinopathy, they appear as a confluent ring around the macula (the macular star).

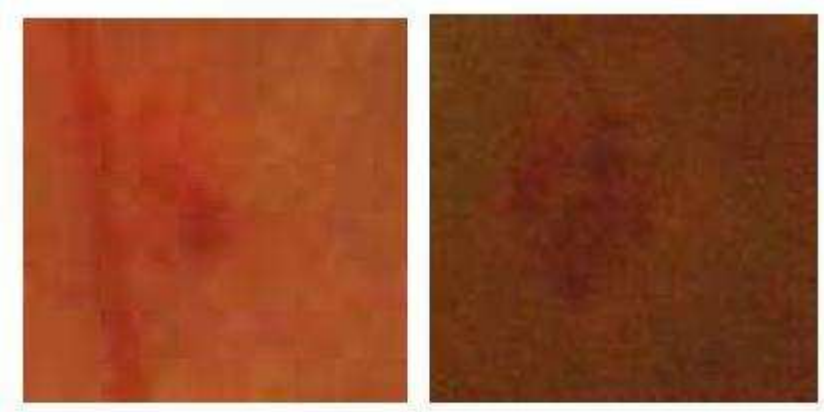

(a) Small hemorrhage (b) Barely visible hemorrhage

(c) Flame hemorrhage

(d) Large hemorrhage

(e) Bright hemorrhage

Figure 2.6: Hemorrhages

2.3.4 Cotton Wool Spots

Cotton wool spots are the consequence of retinal ischemic events, due to precapillary arterioles stenosis. This causes a swelling of the nerve fiber layer, with local deposit of cytoplasmatic material. They are round or oval in shape, white, pale yellow-white or greyish-white, with soft and feathery edges, that give their characteristic aspect and their name. They usually appear along the major vessel arcades, parallel to the nerve fibers, and are sometimes accompanied by the presence of microaneurysms.

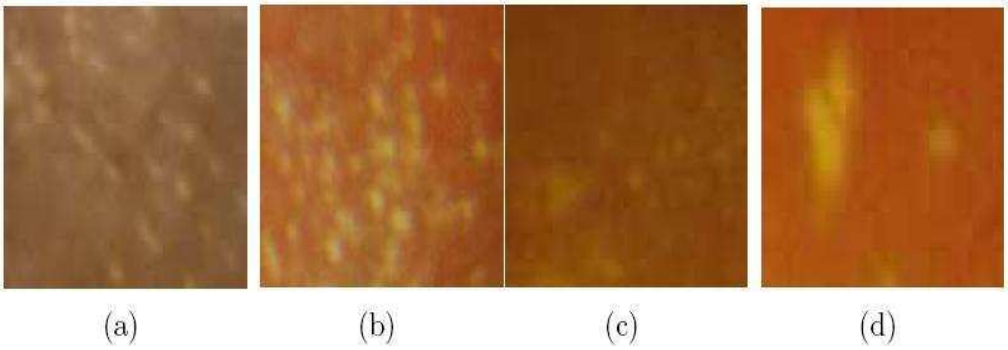

Figure 2.7: Different hard exudates

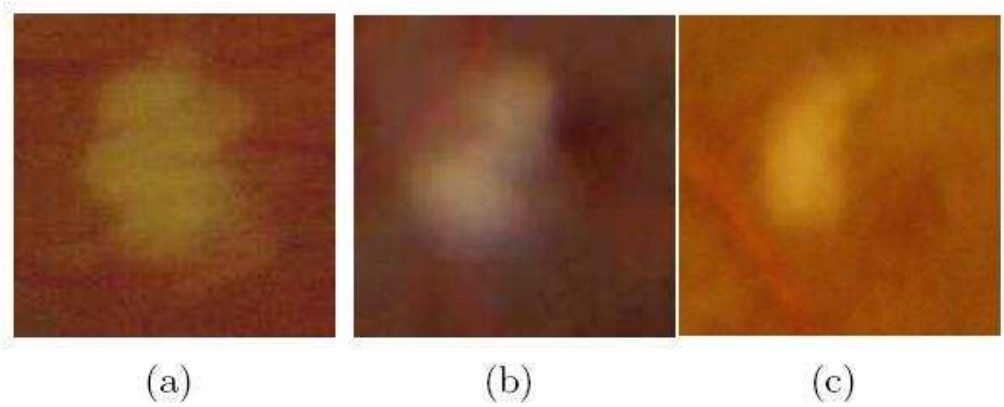

Figure 2.8: Cotton wool spots

2.3.5 Drusen

Drusen are deposits associated with thinning or hypopigmentation of the retinal pigment epithelium. They appear as deep, yellowish-white dots. To distinguish drusen from hard exudates, good stereoscopic view would be necessary, since drusen appear very deep while hard exudates are slightly more superficial. In the protocol used in this thesis the photographs are mono, therefore it is not easy to identify hard exudates from drusen. Several other features are used in distinguishing drusen from hard exudates. Drusen are usually scattered diffusely or scattered near the center of the macula. They are usually round in shape, while hard exudates are usually irregular in shape. Finally, drusen have often a faint border of pigment.

2.4 – Hypertensive Retinopathy

The classification of hypertensive changes in the retina in a severity scale was first proposed by Keith [49], in what is now currently known as the

Keith- Wegener-Barker grading system. It was subsequently modified by Scheie [50] to better separate hypertensive from atherosclerotic abnormalities. In Tab. 2.1 the two classifications for hypertensive retinopathy are shown. It is worth noting that recent literature challenges the prognostic significance of these classifications. The poor correlation with the severity of hypertension variation in the onset and progression of the clinical signs, has suggested the use of a classification of retinopathy into two grades: non-malignant and malignant [51]. This is further confirmed by the fact that density of perifoveal capillaries and capillary blood flow velocity analysed with an angiographic examination, correlate more with a two grade rather than with the classical four grade classification system. Nevertheless, the Keith-Wegener-Barker is
still the standard de facto in the evaluation of hypertensive retinopathy.

Keith-Wegener-Barker		Scheie	
Grade	Features	Grade	Features
I	Mild generalised retinal arteriolar narrowing. Increased arterial tortuosity	1	Barely detectable arterial narrowing
II	Definite focal narrowing and arteriovenous crossing abnormalities	2	Obvious arterial narrowing with focal irregularities and light reflex changes
III	The above and retinal hemorrhages, exudates and cotton wool spots	3	The above plus copper wiring,and retinal hemorrhages and exudates
IV	Severe grade III plus papillar oedema	4	Grade 3 plus silver wire and papillar oedema

Table 2.1: Classification of hypertensive retinopathy as proposed in [49] and [50]

2.5 – Diabetic Retinopathy

Two landmark clinical trials set the standard in grading diabetic retinopathy. They are the Diabetic Retinopathy Study (DRS) [52] and the Early Treatment Diabetic Retinopathy Study (ETDRS) [53]. The ETDRS severity

scale was based on the Airlie House classification of diabetic retinopathy and is used to grade fundus photographs. It has been widely applied in research settings, publications and it has shown satisfactory reproducibility and validity.

Although it is recognized as the gold standard for grading the severity of diabetic retinopathy in clinical trials, its use in everyday clinical practice has not proven easy or practical. The first reason for this is that the photographic grading system has 90 levels, many more more than what is necessary for clinical care. Given the number of levels to consider and the detailed specific definitions of the levels, and the requirement of comparison with standard photographs, it is not surprising that ETDRS grading procedure is diffcult to remember and apply in a clinical setting. Recently, simplified severity scales have been developed in an effort to improve both the screening of patient with diabetes and communication among caregivers. Yet, to overcome this proliferation of ad hoc grading scales, it has been proposed in [54] a Diabetic Retinopathy Disease Severity Scale, in which separate scales were proposed to grade diabetic retinopathy (4 levels) and macular oedema (5 levels). The two scales are summarized in in Tab. 2.2 and Tab. 2.3.

Disease Severity Level proposed in [54]	Findings Observable on Dilated Ophthalmoscopy
No Apparent Retinopathy	No abnormalities
Mild nonproliferative diabetic retinopathy	Microaneurysms only
Moderate nonproliferative diabetic retinopathy	More than just microaneurysms but less than severe nonproliferative diabetic retinopathy
Severe nonproliferative Diabetic retinopathy	Any of the following: more than 20 intraretinal hemorrhages in each of 4 quadrants; definite venous beading in 2 or more quadrants; prominent intraretinal microvascular abnormalities in one or more quadrant and no signs of proliferative diabetic retinopathy
Proliferative diabetic retinopathy	One or more of the following: neovascularization, vitreous or preretinal hemorrhage

Table 2.2: Classification of diabetic retinopathy as proposed in [54]

Disease Severity Level proposed in [54]	Findings Observable on DilatedOphthalmoscopy
Diabetic macular oedema apparently absent	No apparent retinal thickening orhard exudates in posterior pole
Mild diabetic macular oedema	Some retinal thickening or hardexudates in the posterior pole but distant from the center of the macula
Moderate diabetic macular oedema	Retinal thickening or hard exudates approaching the center of the macula but not involving the center
Severe diabetic macular oedema	Retinal thickening or hard exudates involving the center of the macula

Table 2.3: Classification of diabetic macular oedema proposed in [54]
Hard exudates are a sign of current or previous macular oedema. Diabetic macular oedema is defined as retinal thickening and requires a three-dimensional assessment.

Chapter 3

Image Acquisition Protocols and Clinical Evaluation

Since the development of the fundus camera, the ophthalmoscopic examination was the standard procedure for evaluating the state of the retina. In the last 15 years, as the fundus camera took ground in the ophthalmologic practice, issues were raised about the sensitivity and specificity of fundus photographs, and about which acquisition protocols may assure the highest sensitivity and specificity for the early identification of sight-threatening diseases.

The gold standard for fundus imaging is the ETDRS protocol. Its practical usefulness is reduced by the complexity of acquisition procedure for the camera technician, by the complexity of images evaluation for the ophthalmologist, and by the discomfort for the patient involved in the procedure.

It is therefore not commonly used in the clinical practice, but mainly limited to large research studies. As fundus camera quality increases, a number of protocols simpler than ETDRS have been proposed and validated against that gold standard. Even if none has taken solid ground in the clinical practice, the future for the widespread utilization of fundus imaging will be wide angle, few fields photographs protocols. In this chapter a number of protocols proposed in the literature will be presented.

3.1 – Diabetic Retinopathy

The grading of Early Treatment Diabetic Retinopathy Study (ETDRS) seven standard field 35-mm stereoscopic color fundus photographs (ETDRS photos) using the modified Airlie House classification is the current gold standard for determining severity of diabetic retinopathy. The Airlie House Classification of Diabetic Retinopathy provides the photographic basis for

demonstrating the clinical characteristics and extent of clinically pertinent lesions of diabetic retinopathy. Early Treatment Diabetic Retinopathy Study 35-mm retinal photography and grading protocols provide an established and documented sensitivity for detecting and assessing severity of diabetic retinopathy. Compared with other retinal imaging methods, such as Polaroid photography or digital-video imaging, 35-mm slide retinal color photographs have advantages of a large existing database, lower equipment cost, better resolution, and higher color fidelity. Disadvantages associated with 35-mm photography include the requirements for skilled photographers, the need for pupil dilation, uncomfortable examination sessions for the patients, higher costs for film and film handling, delays in film processing, and inefficient archiving with potential for loss or damage of slides. These disadvantages can impact the efficiency, convenience, and cost effectiveness of the procedure and can reduce compliance of patients with annual eye examinations for retinopathy assessment. A number of investigators have evaluated alternatives to ETDRS photos for retinal imaging and assessment of diabetic retinopathy severity.

3.1.1 ETDRS Protocol

The Early Treatment Diabetic Retinopathy Study is built over the Diabetic Retinopathy Study and uses the same protocol of image acquisition. Seven fields, mydriatic, stereoscopic photographs are taken on 35-mm film and subsequently evaluated on light-box. Both for image acquisition and retinopathy grading certified personnel is required. The seven fields are sketched in Fig. 3.1, and described in details in Tab. 3.1. The grading procedure is based on a large set of reference photographs (the standard photographs) for each lesion or abnormality considered. In [53, 48] the complex procedure for classifying the features identified in the set of 7 stereo photographs is reported, together with the gradings to provide the level of retinopathy of the eye under examination.

3.1.2 EURODIAB Protocol

A wide angle retinal photography protocol was developed within the framework of the EURODIAB IDDM Complications Study [55], part of a European Community funded Concerted Action Programme into the epidemiology and prevention of diabetes (EURODIAB). Two 45° colour photographs of each eye are taken. One is centered on the macula, so that the exact centre of the optic disc lay at the nasal end of the horizontal meridian of the field of

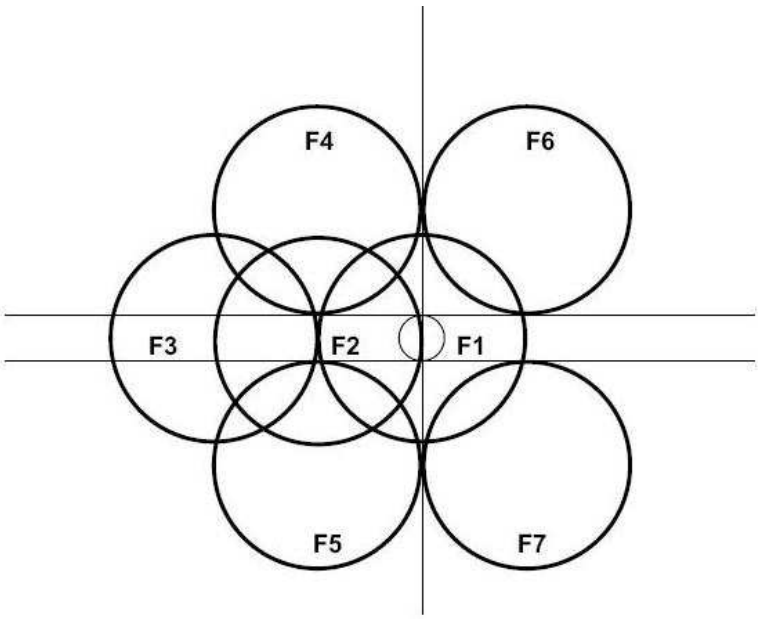

Figure 3.1: Standard ETDRS 7 fields

view. The second is the nasal field, such that the optic disc was positioned one disc diameter from the temporal edge of the field, on the horizontal meridian of the field of view. Considering the partial overlap of the two fields, they provide a retinal view of approximately 80° horizontally by 45° vertically, that the authors judge as suffcient for detecting clinically significant or sight-threatening lesions of diabetic retinopathy. In order to test this, they compared the protocol with the recognised gold standard 7-field 30 degrees stereo photography (assessed using a modified Airlie House classification scheme). It was found that occasionally lesions occurred outside the field of view of either one or the other of the protocol [55].

Simple presence of retinal lesions was correctly detected by both systems in 43 of the 48 eyes, giving 100% agreement on detection. Both systems correctly identified the two known cases of confounding vein occlusion. In eyes with diabetic retinopathy (n = 41), when severity was expressed in three groups: mild background, moderate/severe background and proliferative/ photocoagulated, at least one grader (out of five) using the new system matched the verified results in 38 out of 31 (93%) eyes and three or more graders matched in 31 (76%) eyes. In the view of the authors, the simplicity of application of the system compared to the ETDRS 7-field should prove useful especially in large clinical trials when consistently high quality ETDRS 7-field stereo images would be difficult to achieve.

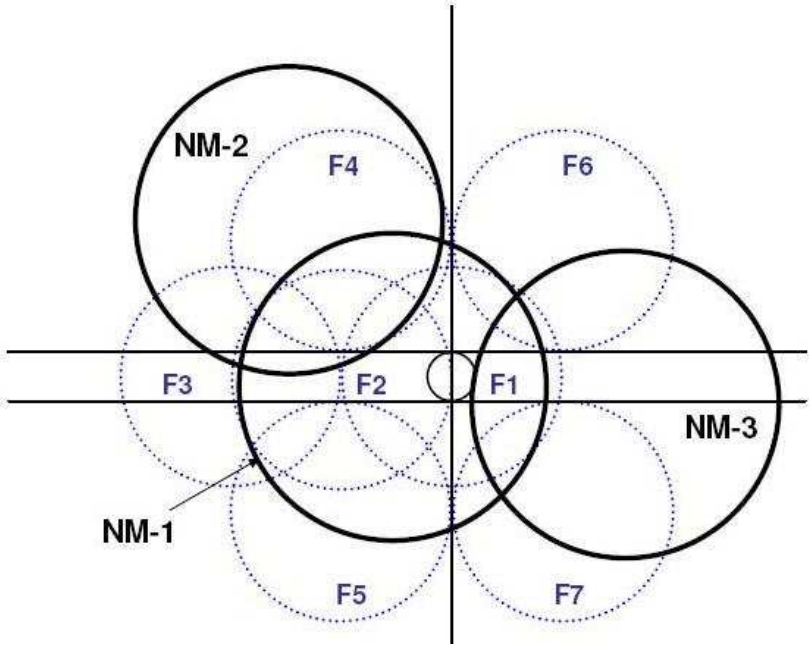

Figure 3.2: Joslin Vision Network Non Mydriatic Fields (black circles), and standard ETDRS 7 fields (dotted blue)

3.1.3 Joslin Clinic Protocol

The Joslin Vision Network (JVN) is telemedicine platform designed to facilitate access of patients with diabetes into the chronic disease management program of diabetes within the Joslin Diabetes Eye Health Care Model.

This system incorporates a commercially available nonmydriatic retinal fundus camera optimized for low-light level imaging of the retina. The protocol [56], developed with the aim of reducing patient discomfort and of

providing an easy picture taking by non-certified photographers, is a three field nonmydriatic 45° photographs. These field are described in Tab. 3.2, and they are represented in Fig. 3.2 superimposed to the ETDRS protocol. This protocol was validated against the ETDRS 30° 7-field stereo. It was demonstrated that the determination of clinical level of diabetic retinopathy using the JVN stereoscopic nonmydriatic digital-video color retinal images from three distinct retinal regions obtained using a 45° nonmydriatic camera optimized for low-lightlevel imaging (JVN images) is in substantial agreement (k =0.65) with dilated ETDRS seven standard field 35-mm stereoscopic 30° retinal photography (ETDRS photos).

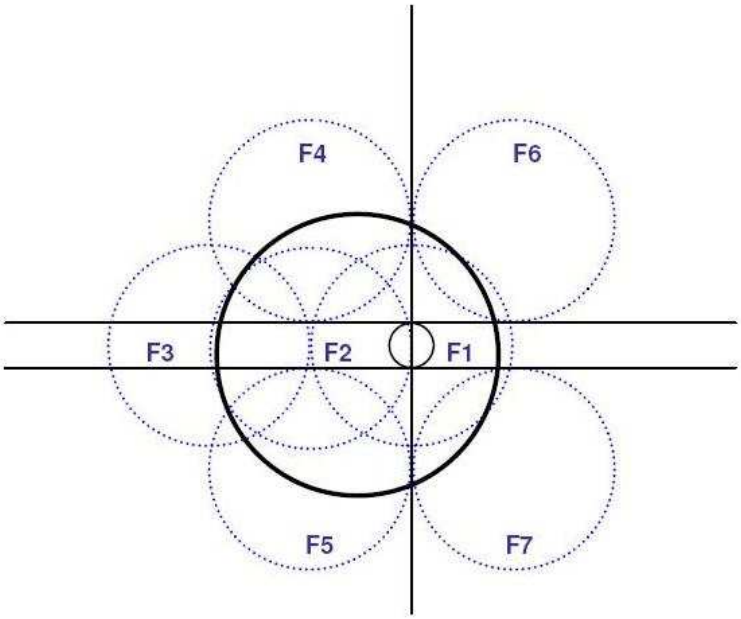

Figure 3.3: Non Mydriatic Monochromatic Field proposed in [57] (black circle), and standard ETDRS 7 fields (dotted blue)

3.1.4 Single Field Monochromatic

In [57], a single wide angle field, monochromatic was tested against ophtalmoscopy conducted by an experienced ophthalmologist and against the ETDRS 7-field stereo. The single field of the 45° photograph was centered on a point halfway between the temporal edge of the optic disk and the fovea, and included areas of the retina on either side of both structures

(Fig. 3.3). Taking the ETDRS retinopathy level 35 as threshold for referral, digital imaging had a sensitivity of 78% and specificity of 86% when compared with standard seven-field color photography.

3.1.5 5-Fields Protocol

In [58] a non-mydriatic digital fundus photography without pupillary dilation, using a non-mydriatic 45 Topcon TRCNW6 fundus camera (Topcon Europe, Rotterdam, The Netherlands), was tested for sensitivity and specificity against the seven ETDRS mydriatic stereo standard fields. in the Early Treatment Diabetic Retinopathy Study (ETDRS) for DR screening.

Five 45° non-stereoscopic images of five overlapping fields were taken for each eye: one image was centered on the macula, including the optic disc, and one each on the nasal, temporal, superior and inferior fields. The sensitivity of detection for moderately severe to severe forms of DR ranged from 92% to 100% and the specificity from 85% to 88%.

3.1.6 Single-Field Colour Protocol

In [59] four screening methods (an exam by an ophthalmologist through dilated pupils using direct and indirect ophthalmoscopy, an exam by a physicians assistant through dilated pupils using direct ophthalmoscopy, a single 45 degrees retinal photograph without pharmacological dilation, and a set of three dilated 45 degrees retinal photographs) were compared with a reference standard of stereoscopic 30 degrees retinal photographs of seven standard fields read by a central reading center. Sensitivity, specificity, and positive and negative likelihood ratios were calculated after dichotomizing the retinopathy levels into none and mild nonproliferative versus moderate to severe nonproliferative and proliferative. The sensitivities, specificities, and positive and negative likelihood ratios are summarized in Tab. 3.3.

In [60], diabetic patients referred for screening were studied in a prospective fashion. A single 45 degrees fundus image was obtained using the nonmydriatic digital camera, and the validation was performed using as ground truth the diabetic retinopathy grading by a consultant

ophthalmologist. The sensitivity for detection of any diabetic retinopathy was 38% and the specificity 95%.

3.2 – Hypertensive Retinopathy

3.2.1 ARIC Protocol

The Atherosclerosis Risk in Communities (ARIC) Study is an epidemiological research study of the major factors contributing to the occurrence and trend of cardiovascular disease in middle-aged adults in the United States. It has two main objectives. Firstly, to investigate factors associated with both atherosclerosis and incidence of clinical cardiovascular disease, and then to measure coronary heart disease occurrence and trends and relate them to community levels of risk factors, medical care and atherosclerosis. Fundus photographs were used to evaluate changes in the retinal vasculature (presumed to be related to hypertension and/or arteriolar sclerosis) that may be prognostic for various cardiovascular outcomes, but other significant retinal conditions will be noted, such as diabetic retinopathy or vascular occlusions.

Within the ARIC study, the protocol consists of one non-mydriatic 45° retinal photograph. The photographs are subsequently sent to the ARIC Retinal Reading Center for assessment of retinal status [61, 62]. To obtain consistent field specification even when non experienced technician take the photographs, the camera used in the ARIC study is provided with a mask on which to align the optic disc. These aligning masks are provided by the Retinal Reading Center and, when, properly attached to the monitor, they position the optic nerve centered from top to bottom and the nasal edge of the optic nerve falls between 1.5-2 optic disc diameters from the nasal edge of the photograph.

3.2.2 Used Protocol for Hypertensive Retinopathy

Several studies (see also [63]) showed that, as a tool to detect vision-threatening retinopathy, single-field fundus photography interpreted by trained readers has sensitivity ranging from 61% to 90% and specificity ranging from 85% to 97% when compared with the gold standard reference

of stereo-photographs of 7 standard fields. When compared with dilated ophthalmoscopy by an ophthalmologist, single-field fundus photography has sensitivity ranging from 38% to 100% and specificity ranging from 75% to 100%. Therefore, although single-field fundus photography is not a substitute for a comprehensive ophthalmic examination, it can serve as a screening tool to identify patients for referral for ophthalmic evaluation and management.

The advantages of single-field fundus photography interpreted by trained readers are ease of use (only one photograph is required), convenience, and ability to detect retinopathy.

ETDRS Field	Field Definition
F-1	Optic Disc: 30*o* field focused centrally on the optic disc
F-2	Macula: 30*o* field focused on the center of the macula
F-3	F-3 Temporal to Macula: 30*o* field focused so the nasal edge of the field crosses the center of the macula
F-4	F-4 Superior temporal: 30*o* field focused so the lower edge of the field is tangent to a horizontal line passing through the upper edge of the optic disc and the nasal edge of the field is tangent to a vertical line passing through the center of the disc
F-5	F-5 Inferior temporal: 30*o* field focused so the upper edge of the field is tangent to a horizontal line passing through the lower edge of the optic and the nasal edge of the field is tangent to a vertical line passing through the center of the disc
F-6	F-6 Superior nasal: 30*o* field focused so the ower edge of the field is tangent to a horizontal line passing through the upper edge of the optic disc, and the temporal edge of the field is tangent to a vertical line passing through the center of the disc
F-7	F-7 Inferior nasal: 30*o* field focused so the upper edge of the field is tangent to a horizontal line passing through the lower edge of the optic disc, and the temporal edge of the field is tangent to a vertical line passing through the center of the disc
F-8	30° field focused outside the seven standard fields

Table 3.1: Early Treatment Diabetic Retinopathy Study Seven Standard Field Definitions, from [56, 53, 48]

JVN Field	Field Definition
NM-1	45° field focused cent€rally between the temporal margin of optic disc and the center of the macula: Center the camera on the papillomacular bundle midway between the temporal margin of the optic disc and the center of the macula. The horizontal centerline of the image should pass directly through the center of the disc. A stereoscopic image is obtained by capturing one image through the left aspect of the pupil opening, shifting the camera laterally, and then capturing a second image through the right aspect of the pupil. A slight delay between the first and second image may be necessary to allow for adequate pupil mydriasis

NM-2	45° field focused superior temporal to the optic disc: Center the camera laterally approximately one-half disc diameter temporal to the center of the macula. The lower edge of the field is tangent to a horizontal line passing through the upper edge of the optic disc. This image is taken temporal to the macula but includes more retina nasal and superior to the macula than standard Field 2
NM-3	45° field focused nasal to the optic disc: This field is nasal to the optic disc and may include part of the optic disc. The horizontal centerline of the image should pass Tangent to the lower edge of the optic disc.
NM-4	45°field focused temporal to the macula (obtained through dilated pupils only)
NM-5	45°any optional field focused beyond the definition s of NM fields 1-4

Table 3.2: Joslin Vision Network Non-mydriatic Retinal Fields

	Ophthalmologist	Physician Assistant	Single nonmydriatic photograph	Three mydriatic photographs
Sensitivity	0.33	0.14	0.61	0.81
Specificity	0.99	0.99	0.85	0.97
Positive Ratio	72	12	4.1	54
Negative	0.67	0.87	0.46	0.19

Table 3.3: Results obtained in [59] for four screening protocols

Chapter 4

Image Collection

The algorithms developed in this thesis have been tested on images acquired with different protocols and instruments.

4.1 – Single Field Photographs

In the clinical routine, when checking the retina for retinopathies, it is common to find wide angle photographs, digital for the newest systems or film for the older, with a varying number of fields, depending on the whim of the taker, and if he/she judges that significant lesions are present in non-standard fields. Nevertheless, the most usual field used as starting point is the one centered on the macula: this is the most important area to check for sight threatening lesions. Combining a macular field with wide angle photograph, it allows to evaluate most of the vascular arcades for abnormalities, and to have available for examination both the macula and the optic disc. Even if photographs are non-stereo, optic disc and macula appearances can suggest and sometimes clearly point out the presence of swellings and oedema.

Images used in this thesis with a single field protocol were acquired with a Topcon TRC 50 fundus camera (Topcon Medical Systems, Japan) with a 50° field of view, non stereo, centred on the macula. Images were saved in digital format with a resolution of 1360 dpi, resulting in 1500x1700 pixel images, with 24 bits per pixel. (Fig. 4.1).

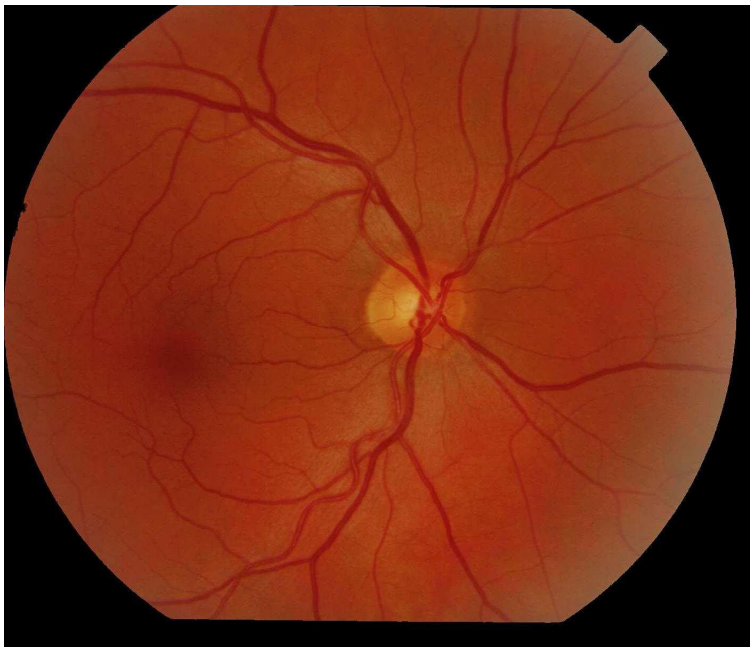

Fig. 4.1: 50° single field photograph

In this thesis some algorithms have been tested with 45° non-mydriatic digital images acquired with Nidek MP1 (Fig. 6.2),resulting in 1392x1038 with 24 bits per pixel.

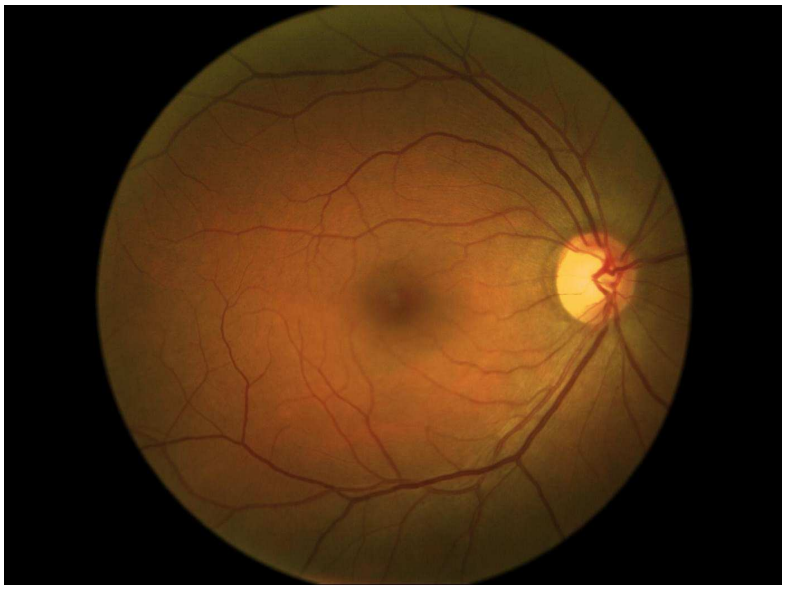

Fig. 4.2: 45° digital image recorded with Nidek MP1

4.2 – 5 Fields Photographs

The algorithms for image mosaicing and fovea identification described in chapter 5 and 8 have been validated on a set of images acquired with the automatic non-mydriatic fundus camera ORION Nidek.

This instrument works without the assistance of an operator taking 5-different fields of the retina with 45° field of view (fig 6.3).

Resolution of each field is 1024x1024 pixels.

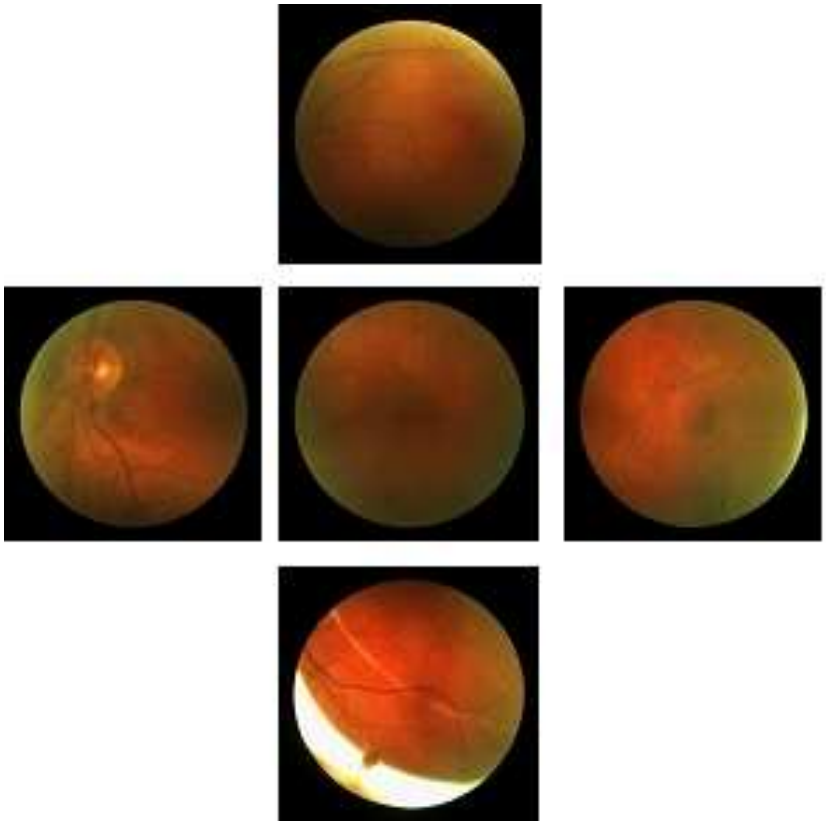

Fig. 4.3: 5 fields recorded with Nidek Orion

Chapter 5

Registration and Mosaicing of Retinal Images

Registration is an essential task in medical imaging, but this is particularly true in retinal analysis, because building a mosaic image from a sequence of partial views is a powerful means of obtaining a complete, non redundant view of a scene.

This is commonly carried out in diabetic retinopathy screening where five or seven fields of view are combined to form a single map of the retina.

This registration generally involves relatively large translation, while there is little rotation due to tilting of the head and through ocular torsion, and little scaling caused by changes in the distance between the camera and the head, due to equipment changes or differing head positions.

5.1 – Review of Available Methods

A broad range of image registration methods have been proposed for different medical imaging applications, including retinal image registration.

Various criteria have been proposed to categorize registration methods [1]–[4].

Typically, retinal image registration techniques are classified as feature-based and area-based methods.

Area-based techniques are generally based on pixel intensities and certain optimized objective functions.

In [6], mutual information is used as a similarity measure and simulated annealing is employed as a searching technique. In [5], the measure of match (MOM) is proposed as an objective function and the genetic algorithm is chosen to be the optimization technique. Nevertheless, the searching space of transformation models (affine, bilinear, and projective) is huge. The greater the geometric distortion between the image pair, the more complicated the searching space.

Feature-based methods are somewhat similar to manual registration. The approach assumes that point correspondences are available in both images, and the registration process is performed by maximizing a similarity measure computed from the correspondences.

The performance of feature-based methods largely depends on sufficient and/or reliable correspondences, especially, when the overlapping part of an image pair is very limited or when there are mismatched correspondences.

A group of papers extract the bifurcations points of the vessels by means of mathematical morphology [8] or Forster detector [9] and then they match corresponding points.

In this chapter will be described a new algorithm that combines the two approaches.

The entire procedure involves two major steps. Translation and rotation between two images are first estimated using Fourier Transforms as in [7] .Then the affine transformation is estimated with a feature-based method that uses the information on rotation and translation obtained with the previous step.

5.2 – Rotation and Translation Estimation using Fourier Transforms

A well-known method for image registration is based on correlation between phase-only versions of the two images to be realigned. This method, covering rigid translational movements, is characterized by an outstanding robustness against noise and disturbances, such as those encountered with non-uniform illumination.

An extension of this method has been proposed in [7] to cover both translational and rotational movements.

5.2.1 Translation Estimation

Let $s_0(x,y)$ and $s_t(x,y)$ represent the two images to be registered and $S_0(\xi,\eta)$ and $S_t(\xi,\eta)$ be their Fourier transforms.

Since in the case of pure translation by (x_0, y_0) $s_t(x,y) = s_0(x-x_0, y-y_0)$,it follows that

$$S_t(\xi,\eta) = e^{-j2\Pi(\xi x_0+\eta y_0)} S_0(\xi,\eta). \qquad (5.1)$$

Therefore, by inverse transforming the ratio of the cross-power spectrum of s_t and s_0 to its magnitudo, $S_t S_0^* / \left| S_t S_0^* \right| = \exp(-j2\pi(\xi x_0 + \eta y_0))$, a Dirac delta distribution centred on (x_0, y_0) is obtained, so that the translation is immediately determined.

5.2.2 Rotation Estimation

If $s_t(x,y)$ is a replica of $s_0(x,y)$, translated by (x_0, y_0) and rotated by θ_0, according to the Fourier Shift Theorem and the Fourier Rotation Theorem their transforms are related by

$$S_t(\xi,\eta) = e^{-j2\pi(\xi x_0+\eta y_0)} S_0(\xi\cos\theta_0 + \eta\sin\theta_0, -\xi\sin\theta_0 + \eta\cos\theta_0).$$

Let us then consider the ratio

$$G(\xi,\eta;\theta) = \frac{S_t(\xi,\eta)}{S_0(\xi\cos\theta + \eta\sin\theta, -\xi\sin\theta + \eta\cos\theta)}, \qquad (5.2)$$

with θ taken as a variable. Obviously , for $\theta = \theta_0$

$$G(\xi,\eta;\theta) = e^{-j2\pi(\xi x_0+\eta y_0)} \qquad (5.3)$$

While, as the difference between θ and θ_0 increases, $G(\xi,\eta;\theta)$ will increasingly differ from this exponential form.

The procedure consists therefore of determining first the angle $\theta = \theta_0$ for which $G(\xi,\eta;\theta)$ reduces to the form (5.3), then in evaluating x_0 and y_0 as in the case of pure translation.

θ_0 can be determined by varying θ until the shape of $g(x, y; \theta)$, the inverse transform of $G(\xi, \eta; \theta)$, gives the closet approximation of a unity pulse (in practice the maximum peak). This can be done rotating the image $s_0(x, y)$ for each tentative values of θ, before transforming.

In practice, for a number of reasons outlined in [10], it is always convenient to use the ration of the cross-power spectrum divided by its magnitude instead of the ratio S_t / S_0.

5.3 – Affine Model Estimation

The registration is refined estimating the affine transformation model with a feature-based scheme.

This transformation maps straight lines into straight lines, whereas it preserves parallelism between lines. In the 2-D case, it can be mathematically expressed as

$$\begin{pmatrix} x' \\ y' \end{pmatrix} = \begin{pmatrix} a & b \\ c & d \end{pmatrix} \cdot \begin{pmatrix} x \\ y \end{pmatrix} + \begin{pmatrix} e \\ f \end{pmatrix} \qquad (5.4)$$

The affine transformation is completely defined by six independent parameters.

5.3.1 Control Points Selection

After rotation and translation estimation, the inverse geometrical transformation is performed on $s_t(x, y)$ obtaining $s_0'(x, y)$.

Then the points in the overlapping area between the two images $s_0(x, y)$ and $s_0'(x, y)$ are sampled in a rectangular grid with step w, and sorted according their contrast in a neighbourhood of size wxw defined as

$$c(x, y) = \sqrt{\frac{1}{w^2} \sum_{k=-w}^{w} \sum_{h=-w}^{w} (s_0(x+h, y+k) - m_{xy})^2} \qquad (5.6)$$

$$m_{xy} = \frac{1}{w} \sum_{k=-w}^{w} \sum_{h=-w}^{w} s_0(x+h, y+k) \qquad (5.7)$$

Then the first 20 points with the highest contrast are chosen as control points.

5.3.2 Control Points Matching

For each control point (x_i, y_i) a region of interest $T_{x_i y_i}(x, y)$ centred in (x_i, y_i) is extracted from the image $s_0(x, y)$ and used as a template to search the correspondent control point (x_i', y_i') in the image $s_0'(x, y)$, searching the point with the highest correlation between the template and the image $s_0'(x, y)$

$$(x_i', y_i') = \arg\max_{(xc,yc)} \sum_x \sum_y T_{x_i y_i}(x, y) \cdot s_0'(x - xc, y - yc) \qquad (5.8)$$

To speed up the algorithm the search is performed only in a little neighbourhood of the point (x_i, y_i). This is possible because we have yet estimated the translation and rotation transformation between the two images.

5.3.3 Model Estimation

The affine transformation $\begin{pmatrix} x' \\ y' \end{pmatrix} = \begin{pmatrix} a & b \\ c & d \end{pmatrix} \cdot \begin{pmatrix} x \\ y \end{pmatrix} + \begin{pmatrix} e \\ f \end{pmatrix}$ for n pair of control points can be written as follows

$$\begin{bmatrix} x_1 & y_1 & 1 & 0 & 0 & 0 \\ 0 & 0 & 0 & x_1 & y_1 & 1 \\ x_2 & y_2 & 1 & 0 & 0 & 0 \\ 0 & 0 & 0 & x_2 & y_2 & 1 \\ . & . & . & . & . & . \\ . & . & . & . & . & . \\ x_n & y_n & 1 & 0 & 0 & 0 \\ 0 & 0 & 0 & x_n & y_n & 1 \end{bmatrix} \cdot \begin{bmatrix} a \\ b \\ e \\ c \\ d \\ f \end{bmatrix} = \begin{bmatrix} x_1' \\ y_1' \\ x_2' \\ y_2' \\ . \\ . \\ x_n' \\ y_n' \end{bmatrix}$$

Let $\varepsilon = \mathrm{A}p - \beta$, the general least square problem is to find a vector p that minimizes the quantity

$$\sum_{i=1}^{n} \varepsilon_i^2 = \varepsilon^T \varepsilon = (Ap - \beta)^T (Ap - \beta) \qquad (5.9)$$

so the least square solution is given by $p = (A^T A)^{-1} A^T \beta$

5.4 – Image Warping and Blending

When the geometrical relationship between the two images to be registered $s_0(x, y)$ and $s_t(x, y)$ is known, the image $s_t(x, y)$ is warped into the spatial domain of the anchor image $s_0(x, y)$ (bilinear interpolation is used to calculate all pixels).

The intensity at each pixel location is the weighted average of all the intensities in the anchor image and in the warped image, falling within a pixel radius.

With the two images mapped into the same coordinate system, the images are combined to form a single visually appealing mosaic with invisible image boundaries.

Ideally, corresponding image pixels should have the same intensity and colour on every image. In practice, however, this is not the case. Possible causes are inhomogeneous illumination, changes in aperture and exposure time.

Therefore we used a blending mask determined by assigning a weight to each pixel in an image that varies from 1 in the center of the image to 0 at the edge.

The choice of this weighting function was inspired by the observation that retina images tend to be more focused in the middle and the illumination gets inferior with increasing distance from the image center.

5.5 – Performance Evaluation

The algorithm described in this chapter has been tested on images acquired with an automatic non-mydriatic fundus camera Orion Nidek.

This camera takes five images representing different fields of the retina, with field of view 45°, and then the acquired images are transferred to a laptop computer for image analysis in order to provide automated detection of diabetic retinopathy.

The first processing step is building a mosaic image from this sequence of partial views to obtain a complete, non redundant view.

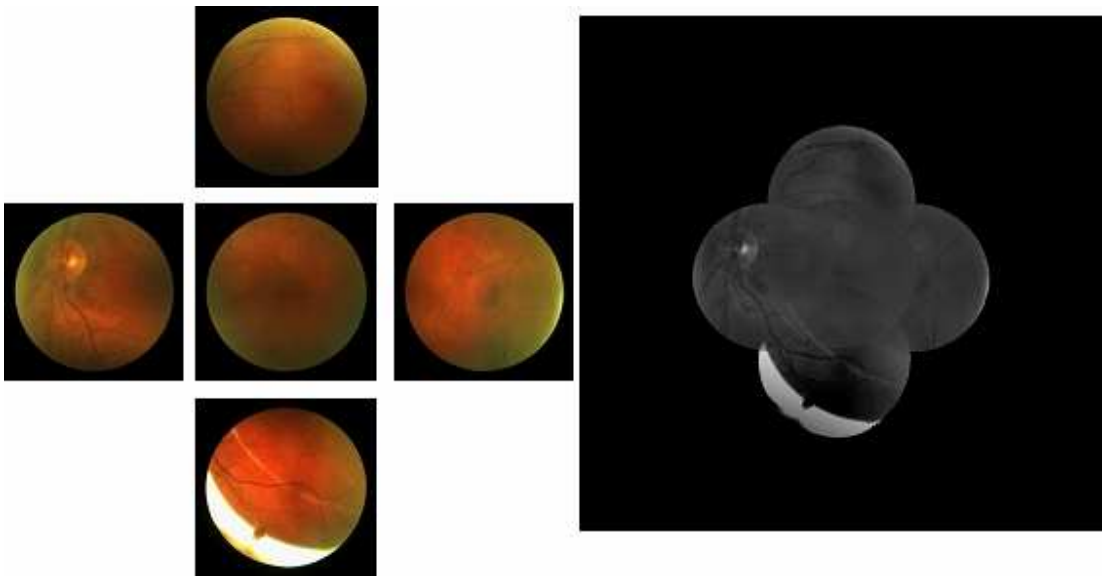

Figura 5.1: five different fields of the retina and the image mosaic

These images can suffer from different problems:

- Out of Focus: cause of the curved retina surface only the central part of the photo is in focus, the rest, especially the boarder regions are out of focus.
- Saturation of some regions, as we can see in figure 5.1. This happen when the the light is reflected by the cornea resulting in those artefacts.

This algorithm has been tested on 110 exams, working on 4 pairs of images to be registered for each exam: central field-superior field, central field-inferior field, central-nasal, central-temporal, with the central field always as anchor image.

The registration failed in 2% of the exams, and in 32% there are slight overlapping errors producing some artefacts on the resulting image, as in figure 5.2.

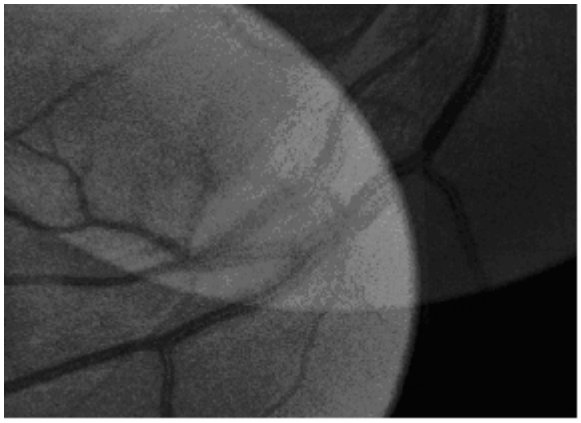

Figure 5.2: slight overlapping errors

We have also compared this method with several other image registration techniques proposed in literature, among which the best results have been obtained with the method described in [11], with 4% of failure rate.

Chapter 6

Automatic Vessel Tracing: detecting false Vessels Recognitions

Automatic tracking of blood vessels in images of retinal fundus is an important and non-invasive procedure for the diagnosis of many diseases. Tracking techniques [41],[42],[21] often present a high rate of false positives.

False trackings can be generated by choroidal vessels running below the retina producing ghost paths through the partially opaque retinal tissue, or by vessel-like structures caused by hemorrhages or exhudates, or by random paths on the fundus pigmentation. Figure 6.1 shows a tracking example and a detail showing an high number of false positives. This problem is more severe when image contrast is poor. In this case it is necessary to reduce the tracking threshold (i.e. the minimum contrast to allow detection) and this may result in an unacceptable amount of false detections. Worse yet, these artifacts are often comparable in caliber and length to true vessels. This chapter presents six methods to discriminate false detections from true positives[45].

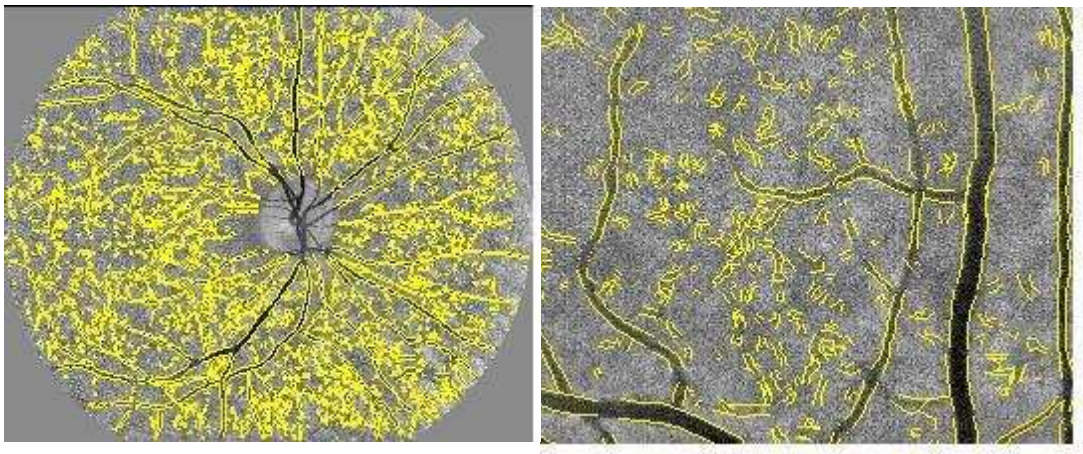

Fig. 6.1: Vessel tracing in a retinal fundus image (left). Cluster of false positive(right)

False positives are very similar to true vessels when observed locally. However, their non-vessel nature appears evident when the whole vessel is considered. Tracking algorithms follow vessel trajectories typically using small observation windows (figure 6.2) in order to neglect curvature.
This results in a large number of false positives. Grayscale and geometric features can be used to define a classification problem that can be solved using a discriminant analysis.

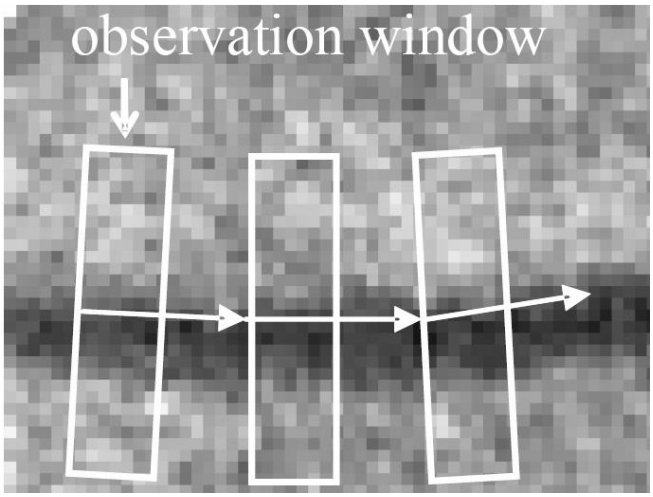

Fig. 6.2: Tracking algorithm observation window. Limited depth is necessary to model vessel borders as straight lines

6.1 – Features Selection

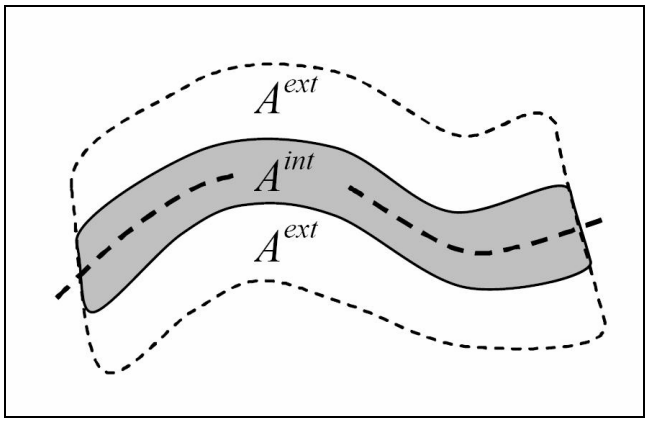

Fig. 6.3: The simplest model divides the vessel in an internal and external area.

The most obvious features are those related to the luminosity (mean) and contrast (variance) of the vessel and of its local background. We define A^{int} the area of image delimited by two vessel borders, and A^{ext} as the background area close to the vessel (figure 6. 3). Internal and external average luminosity and contrast are defined as

$$L^{\text{int}} = \frac{1}{area(A^{\text{int}})} \cdot \sum_{x,y \in A^{\text{int}}} p(x,y) \qquad (6.1)$$

$$L^{ext} = \frac{1}{area(A^{ext})} \cdot \sum_{x,y \in A^{ext}} p(x,y)$$

$$C^{\text{int}} = \frac{1}{area(A^{\text{int}})} \cdot \sum_{x,y \in A^{\text{int}}} \left(p(x,y) - L^{\text{int}}\right)^2 \qquad (6.2)$$

$$C^{ext} = \frac{1}{area(A^{ext})} \cdot \sum_{x,y \in A^{ext}} \left(p(x,y) - L^{ext}\right)^2$$

where p(x,y) is the grayscale value of the pixel at x, y. For an ideal vessel $L^{ext} > L^{\text{int}}$.

The cross-section of a vessel however follows a Gaussian-like profile. The 2-level model poorly accounts for vessel borders.

Silverwire effect (i.e. light reflexion along vessel trajectory due to high reflectance of the vessel walls) also requires more complex models in order to be accounted for. The model is therefore extended by adding a third area, the transition (crossing) area A^{cross}, and the corresponding luminosity and contrast features

$$L^{cross} = \frac{1}{area(A^{cross})} \sum_{x,y \in A^{cross}} p(x,y) \qquad (6.3)$$

$$C^{cross} = \frac{1}{area(A^{cross})} \sum_{x,y \in A^{cross}} (p(x,y) - L^{cross})^2 \qquad (6.4)$$

Intuitively, $L^{\text{int}} < L^{cross} < L^{ext}$, as A^{cross} has pixels from both vessel and non-vessel. For the same reason one expects higher contrast C^{cross} compared to C^{int}, C^{ext}.

This model can be further extended to 4 levels by dividing the cross-section in its internal and external parts with respect to the vessel border, respectively A_i^{cross} and A_e^{cross}. Furthermore, symmetry can be removed by splitting the upper and lower areas with respects to the vessel axis and having corresponding independent features. Upper and lower features are indicated by subscripts u and l. Figure 6.4 shows a schematic diagram of the 2-,3- and 4-level asymmetric models.

Care must be taken in preserving useful information when extending the model. Symmetric external/cross features may provide useful information about texture and structure when combined with their asymmetric counterparts. Symmetric contrast features cannot be computed from the asymmetric ones, therefore they must be included in the feature vectorwhen the model is changed. Accordingly, 3-level cross contrast must be included in the 4-level model feature vector, and four cross-contrast features must be added in the 4-level asymmetric model.

Some relationship can be inferred between vessel contrast and caliber [43,44] and therefore it is reasonable to consider the average vessel calibre μ_Δ as a parameter. Caliber variance Σ_Δ detects any excess variability in caliber that may point out an artifact. Finally, vessel length may improve artifact rejection since many false vessels are shortlengthened.

Table 6.1 shows the gray scale features vector ϕ for the 6 models considered.

Caliber mean and variance and vessel length are included in all models and not shown in table 6.1 for simplicity.

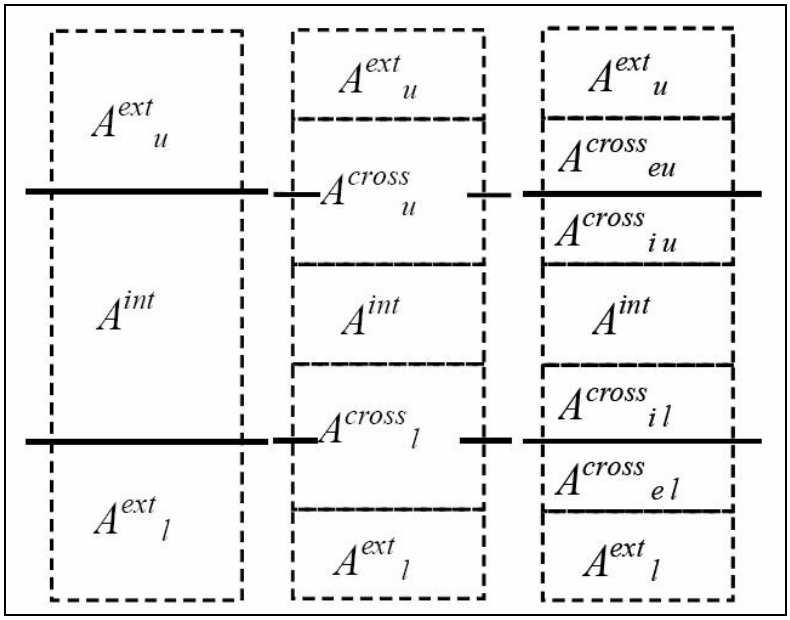

Fig. 6.4: Left to right: 2-, 3-,4-area asymmetric vessel models. Full lines correspond to vessel borders.

2-zones symm	2-zones asymm	3-zones symm	3-zones asymm	4-zones symm	4-zones asymm
L^{int}	L^{int}	L^{int}	L^{int}	L^{int}	L^{int}
L^{ext}	L^{ext}_{u}	L^{cross}	L^{cross}_{u}	L^{cross}_{i}	L^{cross}_{iu}
C^{int}	L^{ext}_{i}	L^{ext}	L^{cross}_{l}	L^{cross}_{e}	L^{cross}_{eu}
C^{ext}	C^{int}	C^{int}	L^{ext}_{u}	L^{ext}	L^{cross}_{il}
	$Cext$	C^{cross}	L^{ext}_{l}	C^{int}	L^{cross}_{el}
	C^{ext}_{u}	C^{ext}	C^{int}	C^{cross}_{i}	L^{ext}_{u}
	C^{ext}_{l}		C^{cross}	C^{cross}_{e}	L^{ext}_{i}
			C^{cross}_{u}	C^{ext}	C^{int}
			C^{cross}_{l}		C^{cross}
			C^{ext}		C^{cross}_{i}
			C^{ext}_{u}		C^{cross}_{e}
			C^{ext}_{l}		C^{cross}_{u}
					C^{cross}_{l}
					C^{cross}_{iu}
					C^{cross}_{eu}
					C^{cross}_{il}
					C^{cross}_{el}
					C^{ext}
					C^{ext}_{u}
					C^{ext}_{l}

Table 6.1: Vessel models and gray scale features vector ϕ

6.2 – Vessel Classification

Once the vector ϕ of features is determined, manually classified data are used to train the linear discriminant w

$$w:\begin{cases} w^T\phi + w_{th} > 0 \Rightarrow \theta \in vessel \\ w^T\theta + w_{th} < 0 \Rightarrow \theta \in non-vessel \end{cases} \quad (6.5)$$

where w_{th} is the threshold parameter. Linear discriminant is trained according to the Fisher discriminant method, which ensures optimal linear separation between the two sets of features by seeking the direction that minimizes interclass cross-variance (i.e. the amount of overlap between two classes).

6.3 – Results

28 retinal images are considered for the experiments. Field of view is 50° and resolution is 1370x1145 pixel. Images include healthy cases as well as pathological ones with exhudates, cotton spots and emorrhages. Luminance and contrast drifts are removed using a normalization method developed in [26]. This pre-processing step also ensures uniform inter-images contrast and luminosity. We have then applied a classification-based sparse tracking algorithm [21] in order to obtain the desired detection of the retinal network. Table 6.2 shows the false vessel ratio expressed as

$$\rho = \frac{length(\,false\ vessels)}{length(\,false\ vessels) + length(true\ vessels)} \quad (6.6)$$

One can see that on average 50% of each tracking is made of false vessels. The proposed methods aim to reduce this figure.

Two parameters are proposed to measure the performance of the false vessel detection algorithm. Sensibility σ measures the ratio between the total length of the true positives TP (false vessels correctly detected) and the total length of the corresponding ground truth GT (total number of false vessels, both detected and undetected). Accuracy α measures the ratio between the total length of true positives and the total length of positives, including false positives FP (i.e. true vessels detected as false).

$$\sigma = \frac{length(TP)}{length(GT)} \tag{6.7}$$

$$\alpha = \frac{length(TP)}{length(TP) + length(FP)} \tag{6.8}$$

The six Fisher discriminants are trained using 14 images (training set), whereas the other ones are used as the validation set. Table 6.3 shows average σ and α after the
application of the six methods proposed.

	training		*validation*	
	mean	*std*	*mean*	*std*
ρ	0.4746	0.0567	0.6256	0.0734

Tab. 6.2: Tracking false vessel ratio

			2-zone	3-zone	4-zone
training	σ	*Symm*	0.7319	0.7879	0.8023
		Asymm	0.7839	0.7515	0.7674
	α	*Symm*	0.9722	0.9638	0.9637
		Asymm	0.9848	0.9720	0.9593
validation	σ	*Symm*	0.4940	0.6164	0.6242
		Asymm	0.6062	0.6160	0.6365
	α	*Symm*	0.9529	0.9704	0.9736
		Asymm	0.8995	0.9476	0.9451

Table 6.3: Sensitivity and accuracy

Chapter 7

Optic Disc Identification

The Optic Disc (OD) is the entrance of the vessels and the optic nerve into the retina (Fig. 7.1) . It appears in color fundus images as a bright yellowish or white region. Its shape is more or less circular, interrupted by the outgoing vessels. Sometimes the optic disc has the form of an ellipse because of a non-negligible angle between image plane and object plane, and its size varies from patient to patient.

From it, the central retinal artery and vein emerge, to cover, with further branching, most of the retinal region. Locating the OD position in fundus images is quite important for many reasons. Many important retinal pathologies may affect the optic nerve. Since the OD may be easily confounded with large exudative lesions by image analysis techniques, its detection is also important to exclude it from the set of possible lesions. Moreover, OD detection is fundamental for establishing a frame of reference within the retinal image and is, thus, important for any image analysis application.

The detection of OD position is also a prerequisite for the computation of some important diagnostic indexes for hypertensive/sclerotic retinopathy based on vasculature, such as central retinal artery equivalent (CRAE) and central retinal vein equivalent (CRVE) [12].

Disc boundary detection is also important to assess the progression of glaucoma, which is due to an increase in intra-ocular pressure and produces additional pathological cupping of the optic disc. The cup-to-disc ratio compares the diameter of the "cup" portion of the optic disc with the total diameter of the optic disc. A cup-to-disc ratio greater than 0.5 is a sign of glaucoma (Fig. 7.2)

In [13] a method based on a model of the geometrical directional pattern of the retinal vascular system is described , which implicitly embeds the information on the OD position as the point of convergence of all vessels.

In this chapter a method to refine the optic disc position estimated with the method in [13] and to estimate the disc diameter will be described .

The estimated position and diameter will be used to initialize an algorithm for the disc boundary detection based on a deformable model based approach.

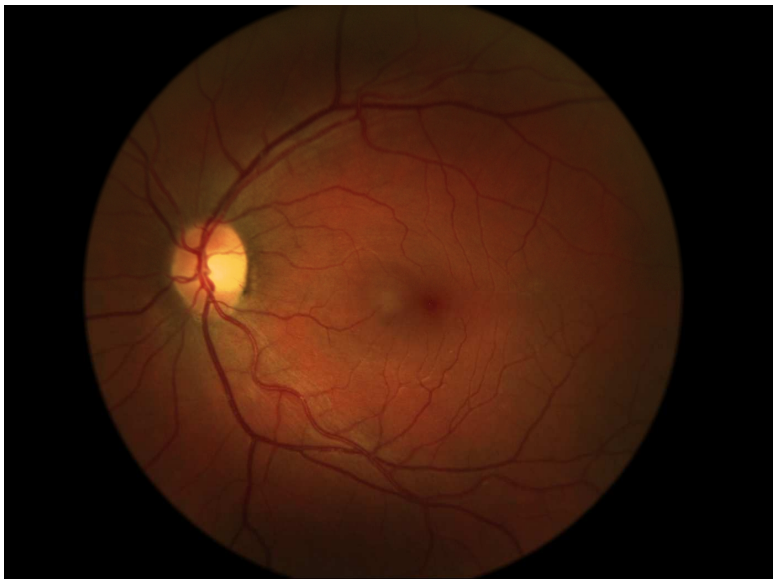

Fig. 7.1: Retinal fundus image with OD (bright round-shape on the left)

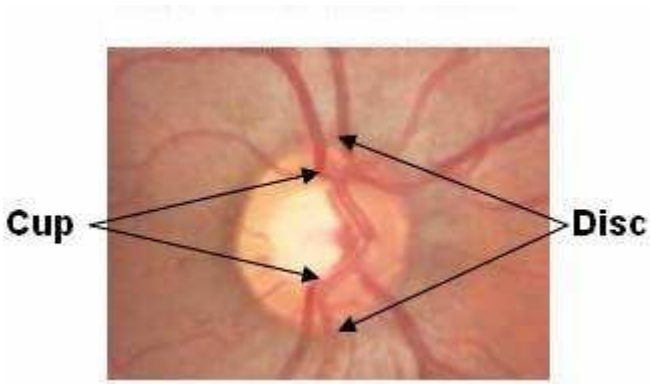

Fig. 7.2: Optic nerve in glaucoma

7.1 – Review of Available Methods

The methods of optic disk boundary detection can be separated into two steps: optic disk localization and disk boundary detection. Correct localization of the optic disk may improve the accuracy of disk boundary extraction.

In [14] the optic disc is localized exploiting its grey level variation. This approach ha been shown to work well, if there are no or only few pathologies like exudates that also appear very bright and are also well contrasted. No method is proposed for the detection of the contours.
A principal component analysis (PCA) model based approach was used in [17], and template matching was used in [18–20].
Foracchia et al. [13] utilized the geometric relationship between the optic disc and main blood vessels to identify the disk location. This method is based on an a geometrical parametric model to describe the general direction of retinal vessels at any given position, where two of the model parameters are the coordinates of the OD center.
In [15] an area threshold is used to localize the optic disc. The contours are detected by means of the Hough transform, i.e. the gradient of the image is calculated, and the best fitting circle is determined. This approach is quite time consuming and it relies on conditions about the shape of the optic disc that are not always met.
In [16] an area threshold is used to localize the optic disc and the watershed transformation to find its contours.

7.2 – Optic Disc Localization

The method of optic disc localization is divided into two steps.
The first step is the algorithm described in [13], which is robust in presence of bright pathologies like exudates. This method requires the preliminary detection of the main retinal vessels using the algorithm proposed in [21], based on a sparse tracking technique.

The second step refines the localization and estimates the optic disc diameter.

7.2.1 Geometrical Model of Vessel Structure

The main vessels originate from the OD and follow a specific course that can be geometrically modelled as two parabolas, with a common vertex inside the OD.

These parabolas can be described as the geometrical locus

$$\Gamma = \left\{(x, y) : ay^2 = |x|\right\} \tag{7.1}$$

On the parabolas the preferential vessel direction is tangent to the parabolas themselves.

In order to completely define the model, it is necessary to express the vessel direction also outside of the parabolic geometrical locus.

Anatomical knowledge indicates that vessels bifurcate when moving away from the OD, and branch vessels tend to diverge from the main vessel. In particular, vessels inside the parabolas quickly bend toward the macula in the temporal region whereas in the nasal region this inward deflection happens at a much slower rate.

Therefore the complete model for vessel direction at any point (x,y) in the image is given by the following equation:

$$\theta^{\mathrm{mod}}(x, y; p) = \arctan\left\{ \frac{\mathrm{sgn}(x - x_{od})\,\mathrm{sgn}(y - y_{od})}{2a\sqrt{\frac{|x - x_{od}|}{a}}} + \frac{(y - y_{od}) - \mathrm{sgn}(y - y_{od})\sqrt{\frac{|x - x_{od}|}{a}}}{\frac{c1}{1 + e^{-(x - xod)}} + \frac{c2}{1 + e^{(x - xod)}}} \right\} \tag{7.2}$$

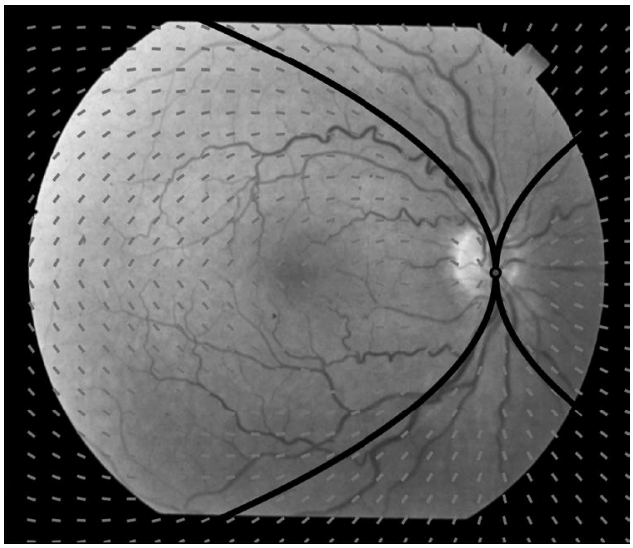

Fig. 7.3:Model of vessel directions

By using suitable model parameter identification techniques, the optimal value for parameters can be identified for any image, given a set of data. The data are the vessel directions measured at points belonging to the vascular structure.

The choice for the identification of model parameters has been the minimization of the weighted residual sum of squares(RSS).

Minimization of RSS with classical gradient-based techniques is rather critical, since this function exhibits many local minima. To overcome this problem, a simulated annealing (SA) optimization algorithm has been adopted.

7.2.2 Position Refinement and Diameter Estimation

The method described above has proved to be very effective, but has the problem to provide as a result a position with a slight offset with respect to the real center of the optic disk.

Furthermore, it is important to have an approximate estimation of the disk diameter to initialize the active contour model .

The gray level profile along the disc radius has a trapezoid shape (fig 7.4), except for the “valleys” created by blood vessels.

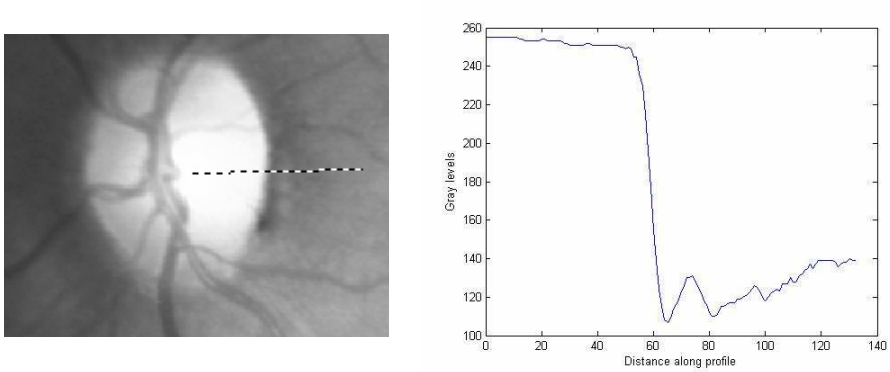

Fig 7.4: Profile along the radius

If the profile $p(x)$ along the radius were a perfect trapezium, the longest of the two parallel side length could be estimated minimizing the function (7.3), as can be observed in fig 7.5.

$$J(r) = \frac{\partial}{\partial r}\left(\frac{\int_0^r p(x)dx}{r} \right) \tag{7.3}$$

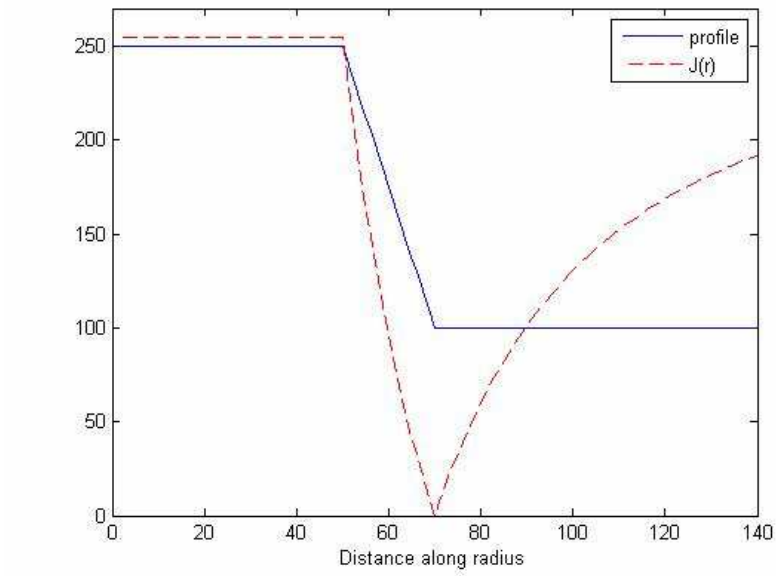

Fig. 7.5: Trapezium side length estimation minimizing the function J(r)

This estimation is robust to noise in the profile because of the integration.

Similarly, a profile $p(x)$ along the OD diameter can be modelled as an isosceles trapezium, and the longest horizontal side length is estimated minimizing the function

$$J(r) = \frac{\partial}{\partial r}\left(\frac{\int_{xc-r}^{xc+r} p(x)dx}{2r} \right) \tag{7.4}$$

with xc the trapezium center coordinate , assumed to be known.

If the trapezium center is unknown, both center and side length can be estimated at the same time minimizing

$$J(r, xc) = \frac{\partial}{\partial r}\left(\frac{\int_{xc-r}^{xc+r} p(x)dx}{2r} \right) \tag{7.5}$$

In fig. 7.6 an example of the estimation of the two parameters xc and r is shown.

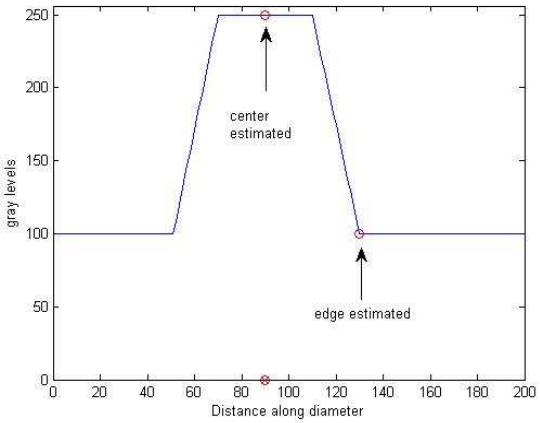

Fig**. 7.6a: Center and border estimation**

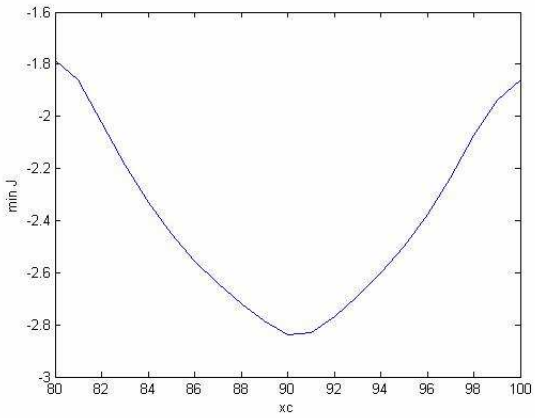

Fig.7.7b: Min J(xc,r) as function of center position xc. $\overline{xc}$ estimated is 90

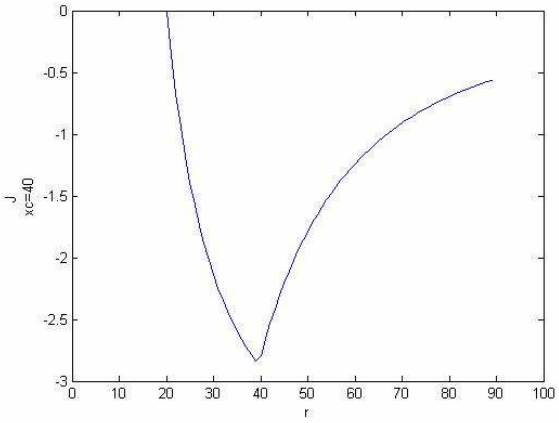

Fig 7.7c: *J($\overline{xc}$, r)* with $\overline{xc}$ = 90 , $\bar{r}$ estimated is 40

Therefore center and diameter of the optic disc can be estimated minimizing

$$J(r, xc, yc) = \frac{\partial}{\partial r}\left(\frac{1}{\pi r^2} \int_0^r \int_0^{2\pi} I_{x_c y_c}(r,\theta) dr\, d\theta \right) \quad , \tag{7.6}$$

$I_{x_c y_c}(x, y) = I(x - x_c, y - y_c)$

$I(x, y)$ *image function* $R^2 \rightarrow R$

x_c , y_c *center's coordinates*

r *radius*

$$\{r_{opt}, x_{opt}, y_{opt}\} = \arg\min_{r,xc,yc} J(r, xc, yc)$$

Fig. 7.8a

Fig. 7.8b

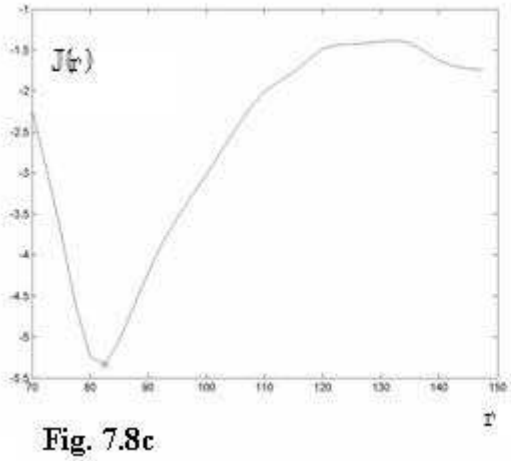

Fig. 7.8c

In fig. 7.8 an example of diameter estimation, minimizing J(r), with center's coordinates assumed to be known.

In practice J(r,xc,yc) is calculated only for (xc,yc) near the position estimated with the parabolic vessel model and for $r_{\min} < r < r_{\max}$.

7.3 – Disc Boundary Detection with Active Contour Models

7.3.1- Active Contour Models ("Snakes")

The active contour model (ACM) algorithm, first introduced by Kass in [22], deforms a contour to lock onto features of interest within in an image. Usually the features are lines, edges, and object boundaries. Kass et al.

named their algorithm “snakes” because the deformable contours resemble snakes as they move.

Given an approximation of the boundary of an object in an image, an active contour model can be used to find the “actual” boundary.

The snake is a contour represented parametrically as $c(s) = (x(s), y(s))$ where $x(s)$ and $y(s)$ are the Cartesian coordinates along the contour and s $\in$ [0,1] is the normalized curvilinear coordinate.

The energy functional to minimize is the sum of two terms:

$$E = \int (\alpha E_{\text{int}}(s) + \beta E_{ext}(s)) ds$$

where E_{int} is an energy function dependent on the shape of the contour and E_{ext} is an energy function dependent on the image properties. α and β are constants providing the relative weighting of the energy terms.

In the discrete case, an ACM is an ordered collection of n points in the image plane:

$$V = \{v_1, \ldots, v_n\}$$
$$v_i = (x_i, y_i),\ i = \{1, \ldots, n\}$$

In [22] the energy functional is minimized using techniques of variational calculus. Amini et al. in [23] have pointed out some of the problems with this approach, including numerical instability and a tendency for points to bunch up on strong portions of an edge contour. They proposed an algorithm for the active contour model using dynamic programming. This approach is more stable and allows the inclusion of hard constraints: however, it is slow, having complexity $O(nm^3)$, where n is the number of points in the contour and m is the size of the neighbourhood in which a point can move during a single iteration.

In [24] a greedy algorithm is proposed , which has performance comparable to the dynamic programming and variational calculus approaches. It retains the improvements of stability, flexibility, and inclusion of hard constraints introduced by dynamic programming but is more than an order of magnitude faster than that approach, being $O(nm$).

In this chapter this greedy approach will be used.

As proposed in [25], a dynamic $\rho - \theta$ polar coordinate system of the optic disk is set up for contour deformation. The starting disc center is estimated

as explained in the previous chapter. The initial contour points are selected at $\rho_i = \bar{r} + 20$, with $\bar{r}$ the radius estimated at the previous step, for every 10^o of θ resulting in N=36 points.

The contour deformation is made possible only along $\pm\rho$ directions.

For each point v_{ik} in the neighbourhood of v_i along $\pm\rho$ directions, an energy term is computed:

$$E_{ik} = \alpha E_{\text{int}}(v_{ik}) + \beta E_{ext}(v_{ik})$$

Then the points iteratively approach the boundary of the OD making locally optimal choices at each iteration, moving towards the final solution which will be hopefully globally optimum.

7.3.2- Internal Energy

The internal energy function is intended to enforce a shape on the deformable contour.

The internal energy function used in this work is defined as follows:

$$\alpha E_{\text{int}}(v_{ik}) = cE_{con}(v_{ik}) + bE_{bal}(v_{ik})$$

Where $E_{con}(v_{ik})$ is the continuity energy that enforces the shape of the contour ; $E_{bal}(v_{ik})$ is a balloon force that causes the contour to grow or shrink; *c* and *b* provide the relative weighting of the energy terms.

$$E_{con}(v_{ik}) = c_1\left|\frac{ds(v_{ik})}{dn}\right| + c_2\left|\frac{d^2 s(v_{ik})}{dn^2}\right|,$$

Where c_1 and c_2 are constants specifying the elasticity and stiffness of the snake.

$$E_{bal}(v_{ik}) = \rho_{vi} - \rho_{vik}$$

7.3.3- External Energy

The magnitude of gradient can efficiently provide the boundary location. Gradient orientation is also considered in the energy function.

$$E_{ext}(v_{ik}) = \beta_1 E_{gradient}(v_{ik}) + \beta_2 E_{ori}(v_{ik})$$

$$E_{gradient}(v_{ik}) = -\left|\nabla I(v_{ik})\right|$$

Let Ori(v_{ik}) denote the gradient orientation at point v_{ik}. Considering that the optic disk is close to a circular shape , the gradient orientation at point v_{ik} should be close to the angle of this point θ_{vi}.

$$E_{orientation}(v_{ik}) = \left|Ori(v_{ik}) - \theta_{vi}\right|$$

7.3.4- Recognition of contour points near blood vessels

It is important to recognize a contour point near blood vessels to avoid the disturbance of the vessel edge.

For each contour point v_i two lines are extracted from the image, one along the direction θ_{vi} and one perpendicular to it.

Then vessel points in these profiles are found by means of a Fuzzy C-Means Classifier (FCM).

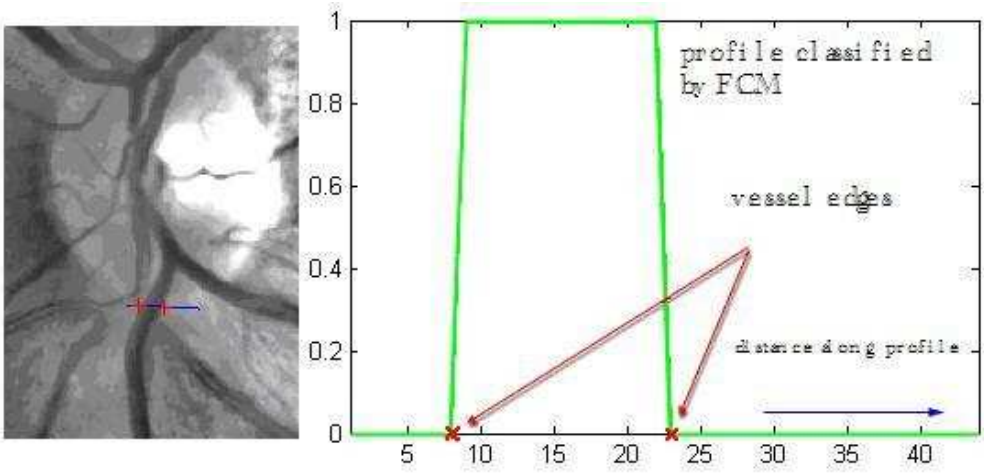

Fig 7.9: Recognition of a blood vessel near a contour point

A contour point near a blood vessel is moved using only the internal energy, to make the algorithm robust against disturbance of the vessel edge.

7.3.5 - Classification of contour points into uncertain-point and edge-point

In each iteration the contour points are classified into uncertain-point and edge-point.

A line along the direction θ_{vi} is extracted and classified with FCM (fig. 7.10).

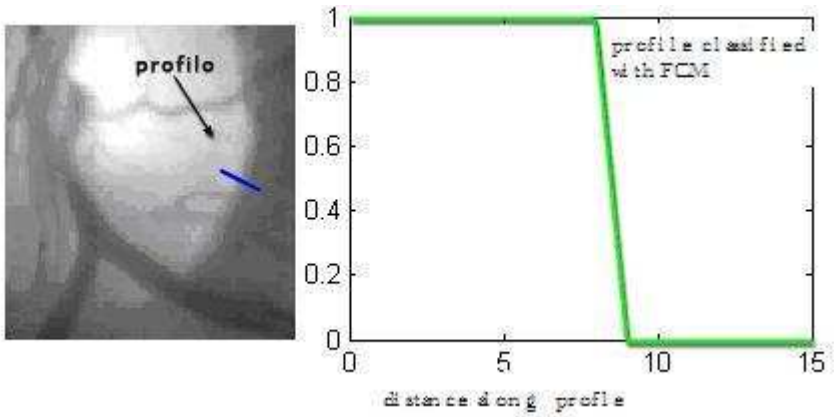

Fig. 7.10: A profile across the optic disc border classified with FCM

The OD center is updated at the end of each iteration according to this classification:

$$xc = \frac{2}{3}\left(\frac{1}{N1}\sum_{i=1}^{N1} x_i^1\right) + \frac{1}{3}\left(\frac{1}{N2}\sum_{i=1}^{N2} x_i^2\right)$$

$$yc = \frac{2}{3}\left(\frac{1}{N1}\sum_{i=1}^{N1} y_i^1\right) + \frac{1}{3}\left(\frac{1}{N2}\sum_{i=1}^{N2} y_i^2\right)$$

where $\{(x_{1,}^1\ y_1^1),(x_{2,}^1\ y_2^1),\ldots,(x_{N1,}^1\ y_{N1}^1)\}$ are the points classified as edge-point and $\{(x_{1,}^2\ y_1^2),(x_{2,}^2\ y_2^2),\ldots,(x_{N2,}^2\ y_{N2}^2)\}$ are the uncertain-points.

7.3.6- Stop Criterion

The average deforming distance in each iteration is used to set the stopping criterion. At iteration k, the average absolute distance between the old contour and deformed contour is defined as

$$AAD(k) = \frac{1}{N}\sum_{i=1}^{N}(x_i^k - x_i^{k-1})^2 + (y_i^k - y_i^{k-1})^2$$

The operation is repeated until the AAD is less than 1 pixel, or until k is less than the maximum number of iterations allowed.

7.3.7- Final classification of reliable contour points.

When the stop criterion is met, the contour points are classified with the method described in 7.3.4 (fig. 7.11).

Then the reliable contour points are interpolated with a spline curve.

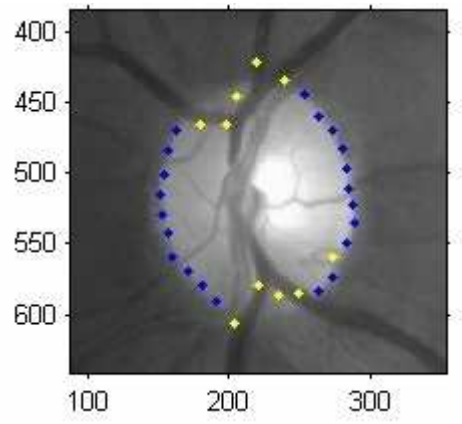

Fig. 7.11: Reliable contour points (in blue)

7.4 – Results

Fourteen 45° color fundus images acquired with Nidek MP1 were tested by the proposed method.

The disk boundary manually marked by a retinal specialist was assumed as the ground truth, and the average distance from the detected boundary point to the ground truth is measured for evaluation.

Tab. 7.4.a shows the results obtained using the green channel(processed to normalize luminosity and contrast [26]) for the vessel recognition step, and using the red channel for the internal energy calculation and contour points classification. This choice was suggested by the fact that the blood vessels are more contrasted in the green channel, while the OD is more contrasted in the red channel.

IMG	Iterations	Final reliable points	Average distance(AD) (Pixels)	AD/(mean OD diameter) %
1	20	23	1,49	1,07%
2	11	22	2,68	1,91%
3	11	25	3,60	1,96%
4	14	26	2,88	1,94%
5	13	28	3,29	2,35%
6	20	22	2,69	2,04%
7	20	24	1,70	1,19%
8	20	15	2,84	2,17%
9	20	15	6,70	4,45%
10	12	12	5,45	3,67%
11	20	24	4,07	2,59%
12	17	13	3,47	2,32%
16	15	22	5,57	3,47%
17	14	28	1,79	1,12%
MEDIA	16,2	21,4	**3,44**	**2,30%**
MAX	20	28	6,70	4,45%
MIN	11	12	1,49	1,07%

Table 7.4.a: Results

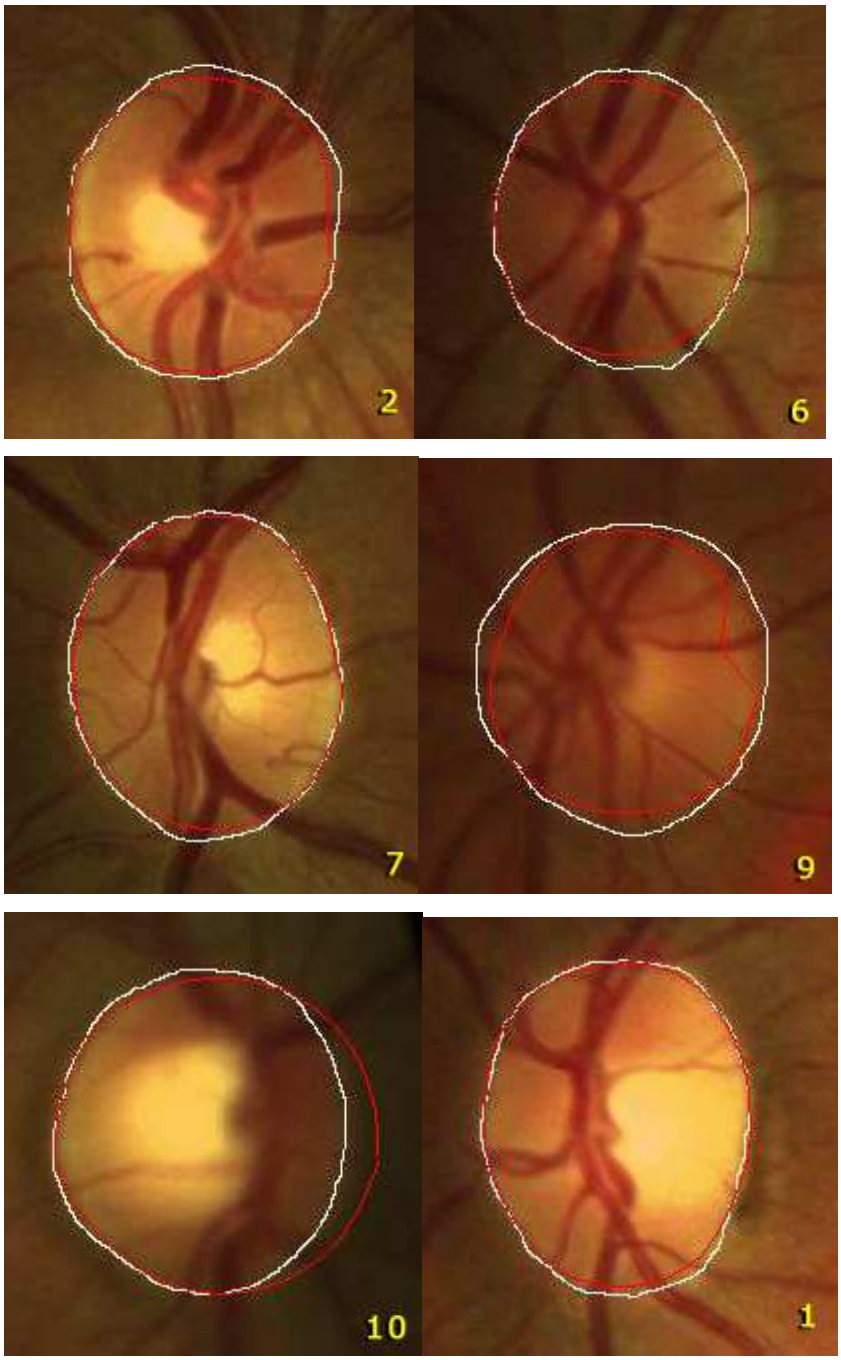

Fig. 7.12: Examples of final snake(red) compared with ground truth (white)

Chapter 8

Fovea Identification

Fovea identification is a fundamental task in any study of ocular diseases, because it is the most accuracy vision zone of the retina, so the nearer the fovea are the more serious the ocular lesions are.

Foveal zone is a small depression at the center of the macula, not fed by retinal vessels, and is indicated by a deep-red or red-brown color. It is temporal to the optic disk (fig. 8.1), and in some images its localization is not obvious due to high illumination or presence of confounding or overlapping lesions.

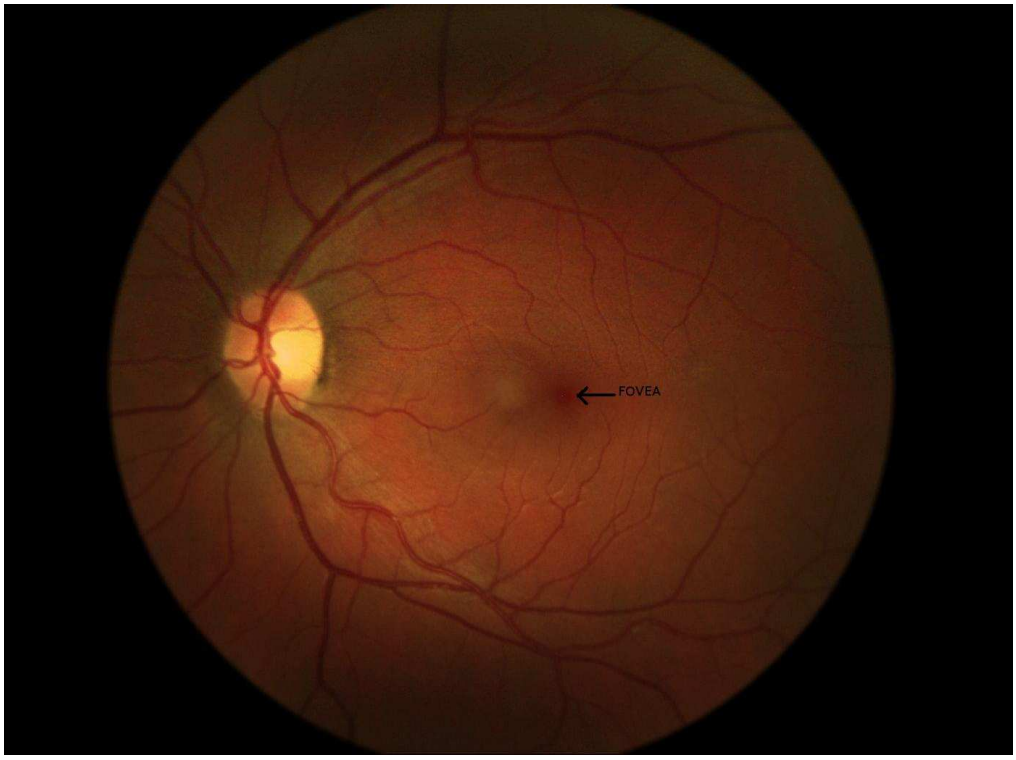

Fig. 8.1: Foveal zone

8.1 – Review of Available Methods

In [27] Ibanez and Simo have proposed a method to detect the fovea exploiting the avascularity and different grey levels at its border.
In [28] the location of the fovea was chosen at the position of maximum correlation between a model template and the intensity image, obtained from the intensity-hue-saturation transformation.
Goldbaum [29] fixed the position of the fovea relative to the optic disc. Li and Chutatape [30] have proposed a method to detect the position of the fovea by extracting the points on the main blood vessels by a modified active model, and fitting a parabola curve with the optic disc as the centre. The fovea is then located at 2 disc diameters from the optic disc on the main axis of the parabola.

8.2 – Geometric Relation between Fovea, Optic Disk and Blood Vessels

The geometrical relation between fovea, optic disk and blood vessels can be exploited to locate the fovea robustly.
Observing the main courses of the blood vessels, their shape is roughly a parabolic curve, with vertex inside the OD and the fovea is situated about at 2 disc diameters from the optic disc along the main axis (fig. 8.2).

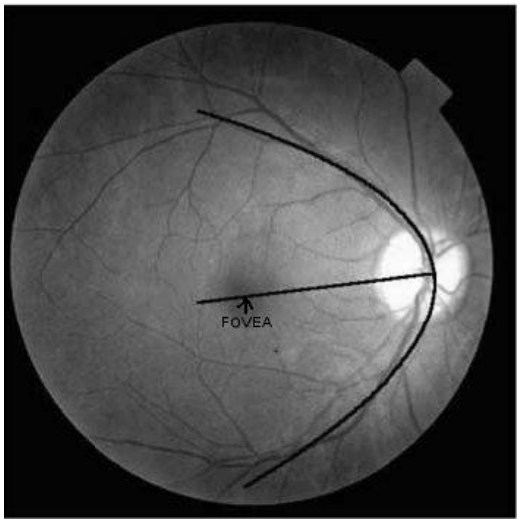

Fig 8.2: Parabolic model of main vessels course

In [30] the main courses of blood vessels are represented by 30 landmark points extracted using an Active Shape Model. Then the four parameters of the parabola (xc,yc,p,θ) , where (xc,yc) is the vertex ,p is the focal length and θ is the rotation of the main axis, are estimated using Hough transform and least square fitting.

This method relies on the correct identification of the landmark points on the main courses of blood vessels, condition not always easily met.

Therefore we have used the more robust method described in 7.2.1 [13] to estimate (xc,yc,p) , fitting a complete model for vessel direction at any point of the image, assuming θ=0.

The data on which the model is fitted are extracted with an algorithm based on a sparse tracking technique [21], which provides vessel's center points and directions.

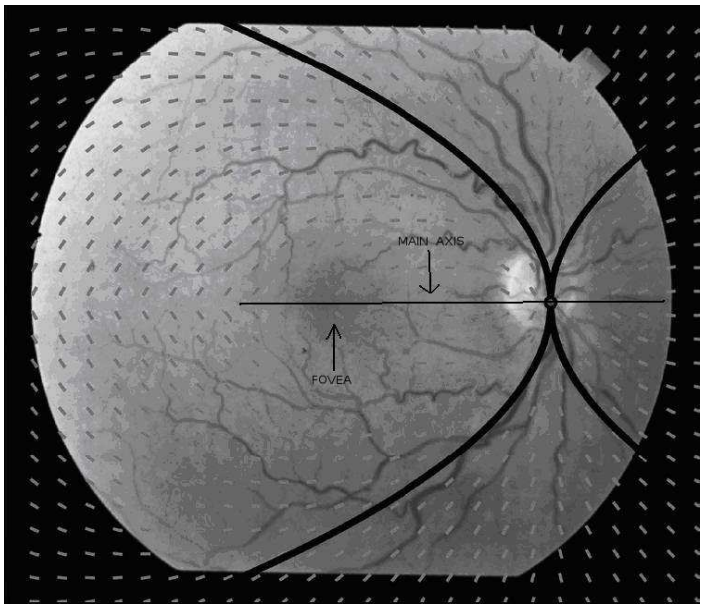

Fig 8.3: Complete model of vessels direction. Model's direction(gray segments) are shown on a grid of points.

8.2.1 Rotation of the Main Axis

We have used a method based on image moments to estimate the rotation of the main axis.

For a greyscale image with pixel intensities I(x,y), moments M_{ij} are defined by

$$f(x,y) = \frac{I(x,y)}{\sum_x \sum_y I(x,y)} \tag{8.1}$$

$$M_{ij} = \sum_x \sum_y x^i y^j f(x,y) \tag{8.2}$$

considering the normalized image f(x,y) as a probability function.

Image orientation can be derived by using the second order central moments to derive the covariance matrix:

$$\Sigma = \begin{bmatrix} \mu_{20} & \mu_{11} \\ \mu_{11} & \mu_{02} \end{bmatrix} \tag{8.3}$$

with μ_{pq} central moments defined as

$$\mu_{pq} = \sum_x \sum_y (x - xc)^p (y - yc)^q f(x,y) dxdy \tag{8.4}$$

where (xc,yc) is the OD center.

The eigenvectors of this matrix correspond to the major and minor axes of the image, so the orientation can be extracted from the angle of the eigenvector associated with the largest eigenvalue.

8.3 – Macula Segmentation using Watershed Transform

The fovea is located at the center of the macula, which is an area not fed by retinal vessels and with a deep-red or red-brown colour , therefore macula segmentation is important to localize the fovea.

There exist two basic ways of approaching image segmentation. The first one is boundary-based and detects local changes. The second is region-based and searches for pixel and region similarities. The watershed transformation belongs to the latter class and is well suited for the segmentation of macula.

8.3.1 Watershed Transform

Considering an image f(x,y) as a topographic surface, catchment basins and the watershed lines can be defined by means of a flooding process.

Imagine that we pierce each minimum of the topographic surface S, and that we plunge this surface into a lake with a constant vertical speed. The water entering through the holes floods the surface S. During the flooding, two or more floods coming from different minima may merge. We want to avoid this event and we build a dam on the points of the surface S where the flood would merge. At the end of the process, only the dams emerge. These dams define the watershed of the function f.

They separate the various catchment basins, each one containing one and only one local minimum of the function (fig. 8.4).

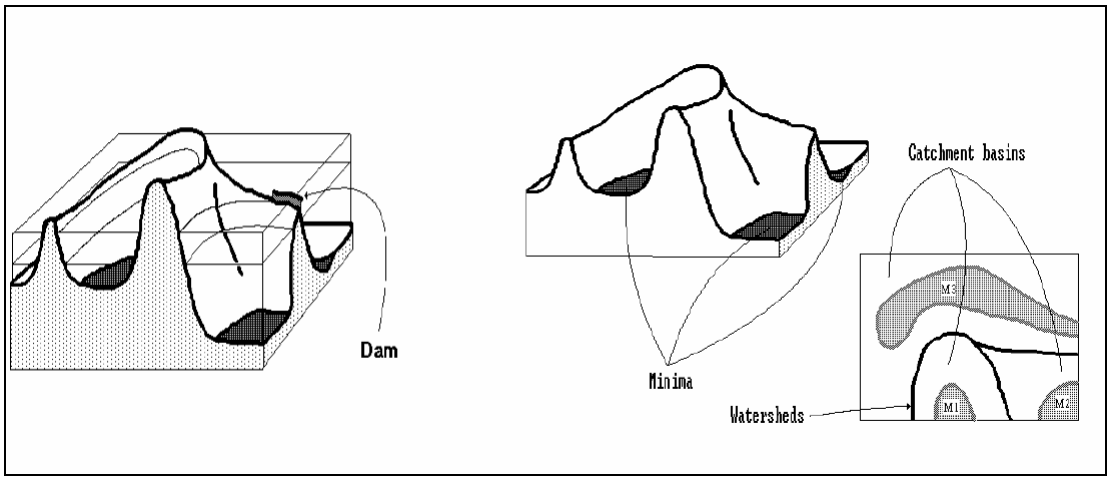

Fig 8.4: Watershed

The watershed algorithms can be divided in two groups. The first group contains algorithms which simulate the flooding process. The second group is made of procedures aiming at the direct detection of the watershed points. These algorithms are detailed in [31]-[33].

8.3.2 Application to Macula Segmentation

In a first step a low-pass filter is applied on the image to remove white noise, that would cause over-segmentation. Then the watershed transform is performed only in a region of interest with size $4 \cdot r_{OD}$ centred in (xf_i, yf_i),

$$xf_i = xc + 4r_{OD} \cdot \cos(\theta)$$
$$yf_i = yc + 4r_{OD} \cdot \sin(\theta) \qquad (8.5)$$

where (xc,yc) is the OD center, r_{OD} is the OD radius and θ the orientation of the main axis.

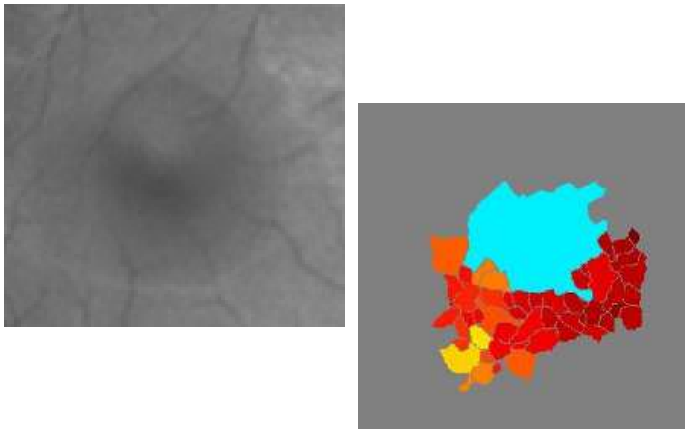

Fig. 8.5: Watershed transform with basins's colour depending on their minimum gray level

The catchment basin with the greatest area is selected as the macula region and its minimum (xf_w, yf_w) is the estimated fovea position (fig.8.6).

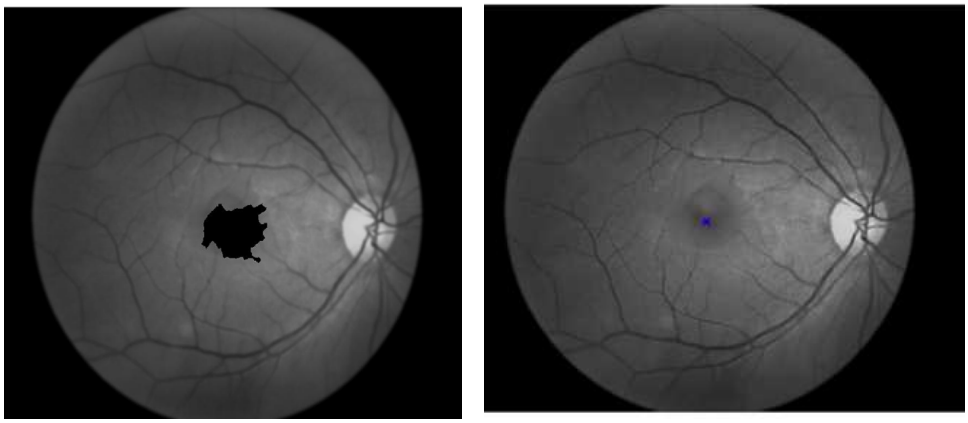

Fig. 8.6: Macula segmentation and fovea detection

8.4 – Fovea Identification with Vascular Analysis

In some images where the foveal zone is covered by lesions or too bright because of high illumination, the method based on watershed transform is proved not to be reliable.

In these cases, a method based only on vascular information and geometric relation with optic disc is more robust.

The method described in [21], based on a sparse tracking technique, is used to extract blood vessels and create the binary image B(x, y) ,where vessel center lines are set to

1 (fig. 8.7).

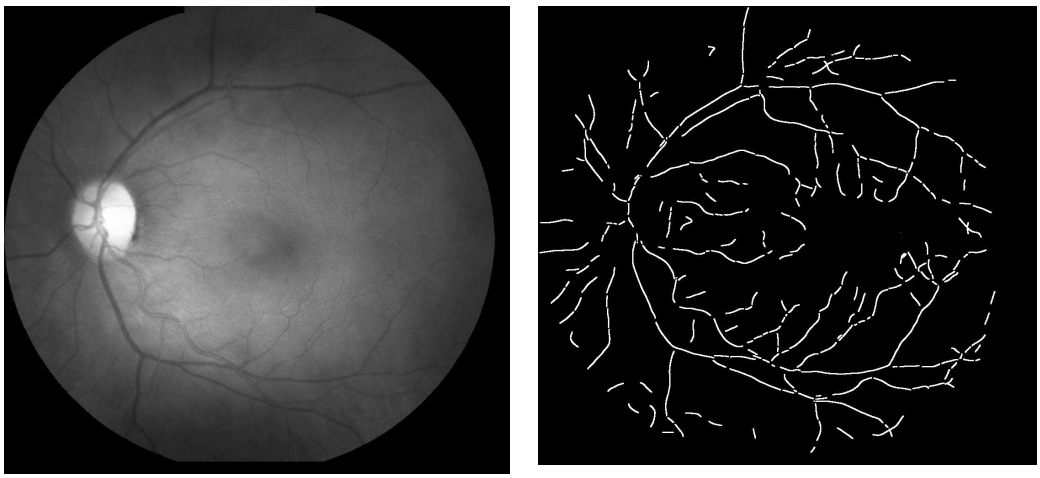

Fig 8.7: Blood vessels segmentation

Then the binary image B(x, y) is convolved with the filter C(x, y) with size Sh x Sk to produce the vascular density VD(x, y)

$$VD(x,y) = \sum_{h=-Sh}^{Sh} \sum_{k=-Sk}^{Sk} B(h,k)C(h-x,k-y) \qquad (8.6)$$

with

$$C(h,k) = \begin{cases} 1 & if \ \left\| h - Sh/2, k - Sk/2 \right\|_2 < 2 \cdot r_{od} \\ 0 & otherwise \end{cases}$$

where r_{od} is the optic disc radius.

Therefore VD(x,y) is the number of blood vessel points inside a circle with radius $2 \cdot r_{od}$ centred in (x,y).

In Fig. 8.8 VD(x,y) is visualized as an image with a colormap ranging from blue (low vascular density) to red (high vascular density).

Fovea (plotted as a circle in fig. 8.8) is then located at the point (xf_v, yf_v) with the lowest vascular density, inside the search area defined in (8.5).

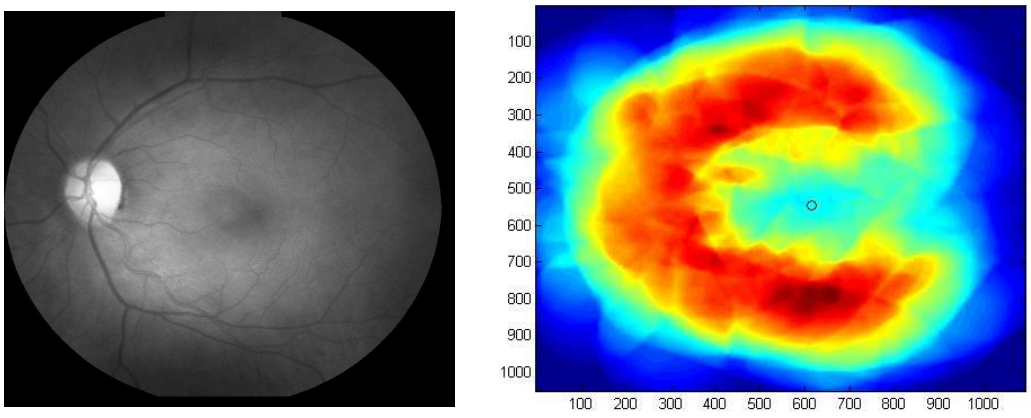

Fig. 8.8: Vascular density and fovea localization

8.5 – Automatic Selection of the Algorithm to be used

The method based on the Watershed transform is robust only if the macula zone is actually a depression in the fundus image (considering the image as a topographic surface). This condition is not always met, for example because may be covered by lesions.

In these cases, it would be better to use the method based on vascular analysis, which however has some drawbacks itself, as it relies on the vessel segmentation and on the vascular tree morphology.

Therefore we have developed a linear classifier to assess whether of the algorithms are reliable by analyzing the outputs in each image .

If both of the methods are classified as reliable, the watershed based output is preferred.

If both of the methods are classified as unreliable, fovea position (xf, yf) is geometrically estimated with an anatomy based algorithm , as follows:

$$xf_g = xc + 4r_{OD} \cdot \cos(\theta) \qquad (8.7)$$

$$yf_g = yc + 4r_{OD} \cdot \sin(\theta)$$

where (xc,yc) is the OD center, r_{OD} is the OD radium and θ the orientation of the main axis.

8.5.1 Reliability of Watershed based Algorithm

A region of interest(ROI) , centred in (xf_w, yf_w), the fovea position provided by the method based on watershed transform, is extracted from the fundus image. Then specific features are calculated and used by a linear classifier to discriminate between two classes: watershed's output reliable or unreliable.

The first step to build a classifier is the feature selection. Given the large number of features that can be computed, there is the need to select the most significant ones, in order to maintain the number of features used by the classifier small, and at the same time keep the discriminating power elevated.

It is important to keep as low as possible the number of features because an increase in computational complexity is not always matched by an increase in discriminatory power or in generalization power.

In order to perform this feature selection, it is necessary to have a measure of the discrimination ability of a set of features. The measure we have used involves the evaluation of intra-class scatter matrix S_w and the inter-class scatter matrix S_b.

Given K classes and a set of features vectors x with dimension N , each one belonging to one and only one class, the intra-class scatter matrix is:

$$S_w = \sum_{i=1}^{K} P(w_i)\Sigma_i \qquad (8.8)$$

$P(w_i)$ is the a priori probability of the class w_i, and Σ_i is its covariance matrix:

$$\Sigma_i = E[(x-\mu_i)(x-\mu_i)^T] \tag{8.9}$$

The inter-class scatter matrix is:

$$S_b = \sum_{i=1}^{K} P(w_i)(\mu_i - \mu_0)(\mu_i - \mu_0)^T \tag{8.10}$$

with μ_0 being the global mean:

$$\mu_0 = \sum_{i=1}^{K} P(w_i)\mu_i \tag{8.11}$$

The function considered as an indicator of the class separation is :

$$J = trace(S_w^{-1} S_b) \tag{8.12}$$

with S_w and S_b defined by (8.8), (8.10).

The NxN matrix $S_w^{-1}S_b$ has rank K-1. The linear transformation mapping the original N-dimensional features space into a new K-1 dimensional space with the same value for J is in fact the matrix having on its columns the K-1 eigenvectors of $S_w^{-1}S_b$.

Using this measure J, we have selected 12 features.

One of the feature is the value of vascular density VD(xf_w, yf_w), as defined in (8.6).

The other features are the first 11 moments M_{pq} of the ROI, as defined in (8.2), $\{M_{00,}M_{10}, M_{01,}M_{11,}M_{21,}M_{12}, M_{22,}M_{31,}M_{13}, M_{32,}M_{23}\}$

The classifier has been trained with 30 images, 15 belonging to the reliable class and 15 to the unreliable class.

S_w and S_b are estimated using the training set, and the eigenvector **w** of $S_w^{-1}S_b$ is calculated.

The output of the linear discriminant analysis is the linear combination of the features with the coefficients of the weighting vector **w.**

8.5.2 Reliability of Vascular Analysis Algorithm

We have also developed a classifier to discriminate between two classes for the vascular analysis 's output , as reliable or unreliable.

The features selected are the first 11 moments of a ROI extracted from the vascular density image VD(x, y) defined in (8.6). The ROI is centred in (xf_v, yf_v), the fovea position estimated with the method based on vascular analysis.

The classifier has been trained with 20 images, 10 belonging to the reliable class and 10 to the unreliable class.

8.6 – Results

	Watershed algorithm	Vascular density algorithm	Geometric algorithm	**Best method chosen by classifiers**
Mean error(pixel)	47.7	60.3	61.5	**35.3**
Std. Dev. error	55.5	45	33.6	**29**
Min error	2.9	1.4	9.2	**2.9**
Max error	296.3	257.9	159.6	**139**

Table 8.1: Performance evaluation on 80 images. Error is the distance from the manually labelled fovea position (in pixel)

The proposed algorithm has been tested on 80 images acquired with an automatic non-mydriatic fundus camera Nidek Orion and processed with the algorithm described in chapter 5 to combine five different fields of view forming a single map of the retina.

Fovea localization in these images have been manually labelled so that ground truth is available for evaluation. In table 8.1 results of the three methods described above are compared with the result achieved using the classifier to select the best algorithm to use for each image.

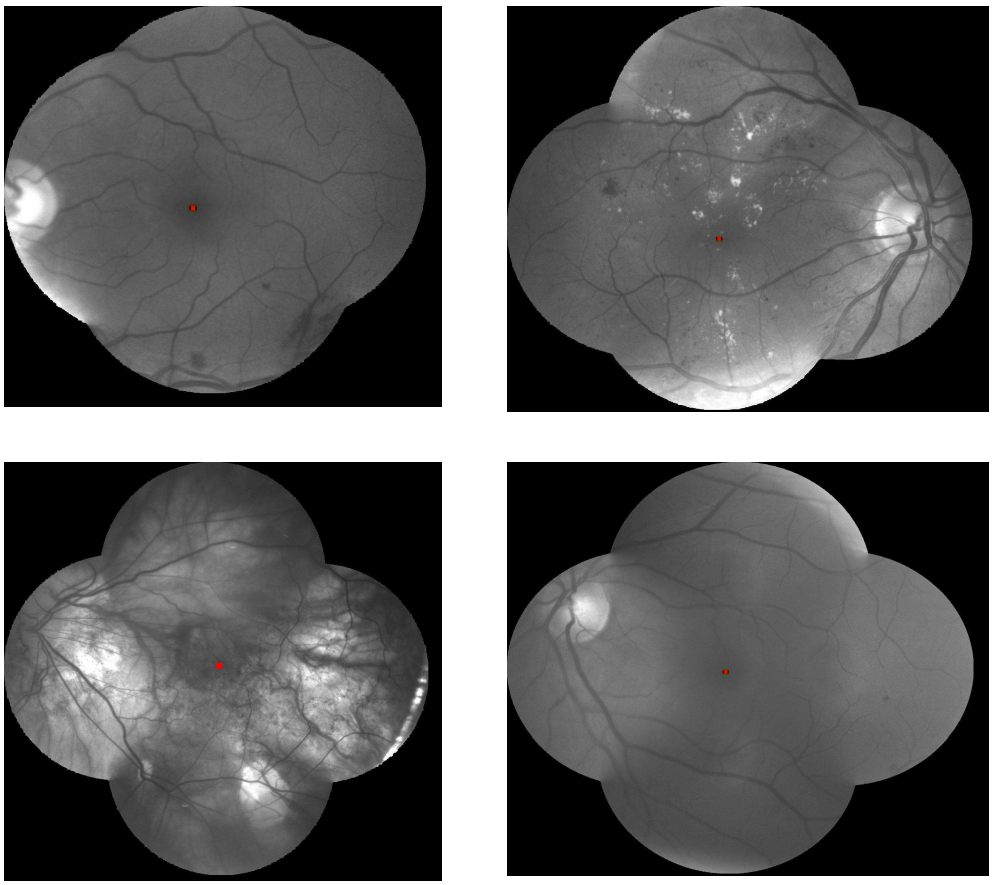

Fig. 8.9: Examples of fovea identification

Chapter 9
Estimation of Generalized Arterioral Narrowing

An early warning about serious cardiovascular diseases can be provided by the analysis of microvasculature health status.

On retinal images, a sign that have been shown to be related to cardiovascular diseases is the generalized arteriolar narrowing, usually expressed by the arteriolar-to venular diameter ratio (AVR) [34]. It is computed from the values of individual arteriolar and venular calibres [35], measured in a specific area of the eye fundus (circular sector around the optic disc).

9.1 – Review of Available Methods

The current procedure requires the long and cumbersome manual measurements of the required vessel calibers. To overcome this problem, computer assisted procedures have been proposed [36], which however still require considerable user assistance. Recently, an automatic system has been reported[37], but it still requires user input for some of the steps, e.g. for artery vs. vein discrimination. In this chapter will be proposed a system for AVR estimation that is completely automatic [40].

9.2 – Preliminary Steps

The fully automatic procedure to derive the AVR index requires several steps to be performed. After an initial image enhancement to improve and normalize image quality, the network of retinal vessel is traced and the optic disc position and diameter are identified. With this information, the specific area in which caliber measurements are to be done is identified. Inside this area, vessels are labeled as either arteries or veins and their caliber is measured. Finally, caliber measurements are used to compute AVR, according to both the standard formula [35] and a more recent revised formula [38].

9.2.1 Image Preprocessing

Very often retinal images are unevenly or non-uniformly illuminated and thus exhibit local luminosity and contrast variability. This problem may seriously affect any diagnostic process and its outcome, especially if an automatic computer-based procedure is used to derive the diagnostic parameters.

To overcome this problem, is used a method to normalize luminosity and contrast in retinal images, both intra and inter image[26]. The method is based on the estimation of the luminosity and contrast variability in he background part of the image and the subsequent compensation of this variability in the whole image.

9.2.2 Vessel Tracing

The identification and quantitative description of the vascular structure is a necessary prerequisite to compute AVR.

To this end, a system for the automatic extraction of the vascular structure in retinal images proposed in [21] is employed , which works on the green channel of the retinal image and is based on a sparse tracking technique. Starting from a set of seed points, the tracking procedure moves along the vessel (Fig. 9.1) by analyzing subsequent vessel cross sections (blue segments in Fig. 1) and extracting the vessel center, caliber and direction. The pixels belonging to the vessel in a cross-section (red segments in Fig. 1) are found by means of a fuzzy C-means classifier applied to all cross-section pixels.

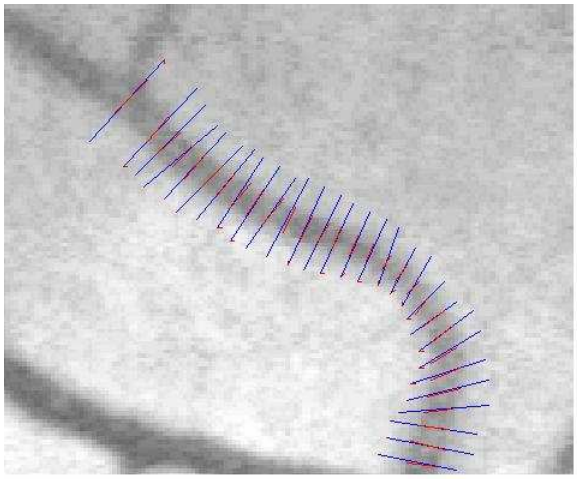

Fig. 9.1: Vessel tracking technique.

9.3 – Roi Detection

The AVR value is computed from the values of individual arteriolar and venular calibers measured in the vessels present in a specific ROI of the eye fundus: a circular sector centered on the optic disc (OD) and from half-disc to one disc diameter from the OD margin (area between dashed lines in Fig 9.2). The OD position needs thus to be detected. The method we used [13] exploits the detection of the main retinal vessels by means of the vessel tracking procedure just summarized. All retinal vessels originate from the OD and then follow a parabolic course towards retinal edges (see Fig. 9.2). A geometrical parametric model was proposed to describe the direction of these vessels and two of the model parameters are just the coordinates of the OD center. Using samples of vessels directions (extracted from fundus images by the tracking procedure) as experimental data, model parameters were identified by means of a simulated annealing optimization technique. These estimated values provide the coordinates of the center of OD. The OD diameter was assumed to be the standard value of 1850 μm [38], and this value was also used to determine the pixel/μm calibration, as established by the Early Treatment Diabetic Retinopathy Study. From the knowledge of OD center and diameter, the circular area for AVR computation can thus be identified on the retinal images.

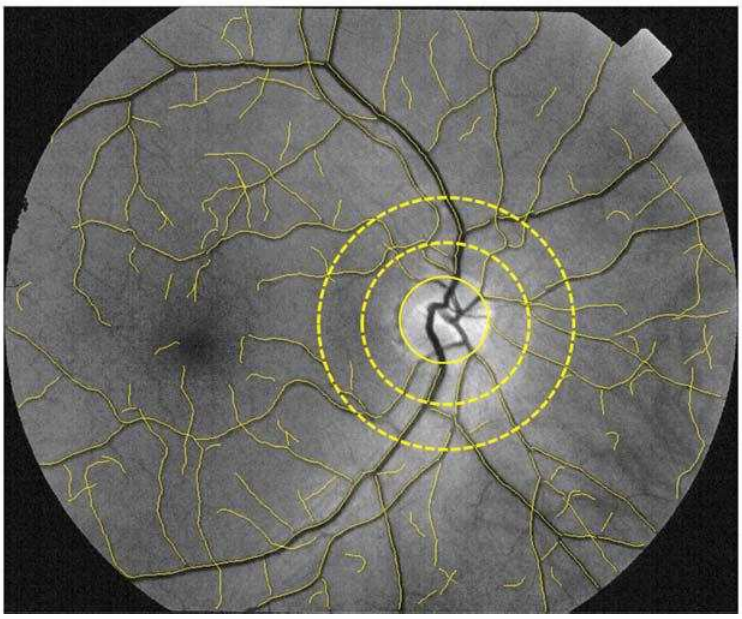

Fig. 9.2. Retinal image with vessel traced by the automatic algorithm. The optic disc contour is shown with solid line and AVR is computed from vessels inside in the circular area contained within the dashed lines.

9.4 – Artery-Vein Discrimination

Individual arteriolar and venular calibers in the ROI are necessary to derive AVR, and thus each traced vessel inside the ROI must be correctly labeled as either artery or vein.

The problem is complicated by the similarity in the descriptive features of these two structures and by the contrast and luminosity variability within and between retinal images.

We have used an algorithm for classifying vessels proposed in [39], which exploits some peculiarities of retinal images, such as the symmetry of the vessel network and the similarity in the number of veins and of arteries.

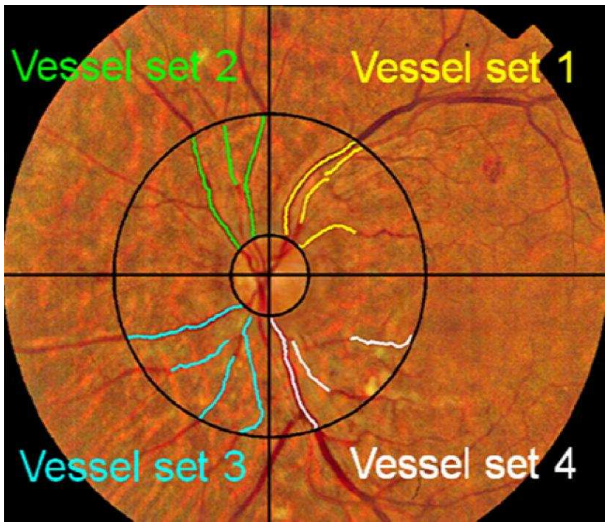

Fig. 9.3: Retinal image with quadrants for A/V discrimination

As only vessels close to each other can be reliably recognized as arteries or veins by direct comparison, without any further semantic knowledge, the classification procedure should have a local nature. A concentric zone around the OD is partitioned into four quadrants and the A/V discrimination is separately performed for the vessel sets in each quadrant (Fig. 3).

The A/V discrimination is based on the local comparison of vessel color features. More specifically, for each vessel sample point a circular neighbourhood of radius dependent on the vessel caliber is considered. The mean of the hue values of the pixels belonging to this neighborhood, and the variance of their red values are the features considered for vessel classification.

In every quadrant, a fuzzy C-mean classifier labels the sample points as either artery points or vein points. From these assignments, an empirical probability P for each vessel segment to be an artery (or vein) can be determined and the highest probability determines the vessel labeling.

9.5 – AVR Estimation

From the arteriolar and venular calibers estimated as described above, the Central Retinal Artery Equivalent (CRAE) and Central Retinal Vein Equivalent (CRVE) parameters can be computed and finally their ratio:

$$AVR = \frac{CRAE}{CRVE}$$

provides an indication of a possible generalized arteriolar narrowing [35,38]. An AVR value smaller than 1 indicates an arteriolar diameter on average narrower than the venular one.

9.6 – Results

Fourteen color retinal images were acquired in normal and hypertensive subjects with a Topcon TRC 50 fundus camera (Topcon Medical Systems, Japan) with a 50° field of view. Images were saved in digital format with a resolution of 1360 dpi, resulting in 1500x1700 pixel images, with 24 bits per pixel.

The reference values, against which the automatic results were to be compared, are the results of a manual AVR estimation. This latter was carried out by manually performing all steps on the retinal image displayed on a PC monitor: identification of OD and its diameter (and thus of the ROI for caliber estimation), vessel labelling as arteries or veins, vessel diameters measurement by drawing segments with the mouse and computing their pixel length. Both the standard [35] and the revised [38] formulas were used to derive AVR values from the arteriolar and venular diameters.

Table 9.1 presents the manual and automatic AVR results obtained in the data set of 14 retinal images, using both the standard and the revised AVR formula, with scatter-plots showing their correlation reported in Fig. 9.4, top and bottom panel respectively. The automatic procedure appears to behave better with the standard formula than for the revised one as regards correlation, 0.83 vs 0.73, whereas automatic/manual ratios have identical average and standard deviations but different range.

A good correlation was found between automatic and manual AVR values when using the standard formula.

Two outliers significantly affect the overall performance (see Fig.9.4). A semi-automatic procedure was then carried out, where selected steps were manually performed in order to identify the reason for the unsatisfactory performance in these images. From this investigation, it appears that vessels missed by the tracing procedure and faulty A/V discrimination are the main reasons for these unsatisfactory performances. The revised formula provides

a slightly worse correlation, but with a much more homogeneous behaviour , as no outliers are evident in the scatter-plot and automatic/manual ratios exhibit a narrower range.

Image	Standard formula			Revised formula		
	Man	Aut	Aut/Man ratio	Man	Aut	Aut/Man ratio
PD56-3	0.50	0.56	1.12	0.45	0.42	0.93
131703-21	0.56	0.60	1.06	0.45	0.49	1.08
PD14-3	0.61	0.62	1.01	0.49	0.51	1.04
PD44-1	0.65	0.86	1.32	0.49	0.60	1.23
8766-7	0.68	0.68	1.00	0.55	0.55	1.00
8759-7	0.70	0.77	1.10	0.55	0.62	1.12
PD68-1	0.72	0.68	0.96	0.49	0.55	1.13
PD01-1	0.78	0.79	1.02	0.62	0.56	0.89
PD36-3	0.79	0.62	0.78	0.53	0.45	0.86
PD07-1	0.82	0.79	0.97	0.67	0.60	0.88
8765-11	0.86	0.89	1.04	0.61	0.64	1.04
PD21-1	0.89	0.95	1.07	0.58	0.64	1.11
131703-09	0.95	0.85	0.89	0.64	0.62	0.97
PD02-3	1.05	1.05	1.00	0.68	0.70	1.03
Mean	**0.75**	**0.76**	**1.02**	**0.56**	**0.57**	**1.02**
Std Dev	**0.15**	**0.14**	**0.12**	**0.08**	**0.08**	**0.11**
Min	**0.50**	**0.56**	**0.78**	**0.45**	**0.42**	**0.86**
Max	**1.05**	**1.05**	**1.32**	**0.68**	**0.70**	**1.23**

Table 9.1: AVR values from the standard and the revised formula. Values obtained with the manual and the automatic procedures and their ratio are reported.

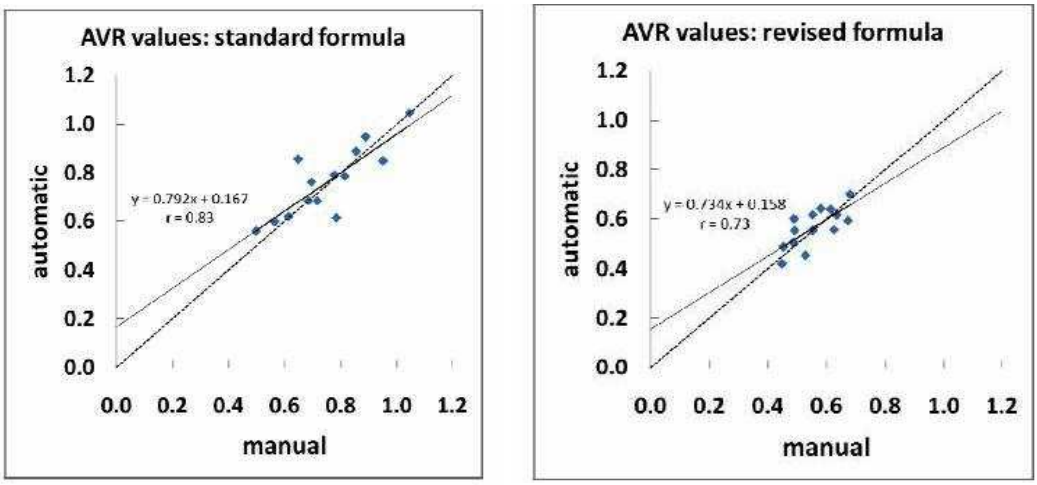

Fig. 9.4: Scatter-plots of AVR values estimated with the standard (top panel) and revised(bottom panel) formula. Regression line(solid) and equation, with correlation coefficient, and identity line (dashed) are shown.

Chapter 10

Conclusions

10.1 – Achieving the Objectives

The aim of this thesis was to develop a set of new algorithms to help ophthalmologist's diagnosis and to be used in automated systems for retinopathy screening. The achievements will be summarized in the following sections.

10.1.1 Mosaicing of Retinal Imaging

Building a mosaic image from a sequence of partial view is a powerful mean of obtaining a complete, non redundant view of a scene. In this thesis a new algorithm was proposed to solve the problem of combining five fields of view to form a single map of the retina.

This registration generally involves large translations, while there is little rotation and scaling. The algorithm proposed involves two steps. Translation and rotation between two images are first estimated using Fourier Transform. Then the affine transformation is estimated with a feature-based method that uses the information on rotation and translation obtained with the previous step.

This algorithm has been tested on 110 exams, working on 4 pairs of images to be registered for each exam: central field-superior field, central field-inferior field, central-nasal, central-temporal, with the central field always as anchor image. Translation and rotation estimation is proved to be robust to noise and blur, with only 2% of failure rate, outperforming other methods described in literature.

In 32% of the exams there are slight overlapping errors producing some artefacts on the resulting image.

10.1.2 Detecting false vessel recognition

Tracking techniques for blood vessels segmentation often present a high rate of false positives. In this thesis a linear classifier was employed as a postprocessing step to remove false positive vessels and improve the specificity of the whole segmentation algorithm.

Six different vessel's models are compared in terms of sensibility and specifity.

Results show an overall good detection of false positives at a marginal cost in terms of discarded true vessels. Increasing model complexity generally increases both sensibility and accuracy. In particular, the 4-level asymmetric model provides the best performance in terms of sensibility, whereas the 3-level asymmetric model shows more uniform performance

10.1.3 Optic Disc Identification

Locating the optic disc position in fundus images is quite important to exclude it from the set of possible lesions, to establish a frame of reference within the retinal image important and possibly to assess the progression of glaucoma, which is due to an increase in intra-ocular pressure and produces additional pathological cupping of the optic disc.

In this thesis a method to refine the optic disc position estimated with a previously developed method and to estimate the disc diameter was described. This algorithm is based on an active contour model, modified to be robust to disturbance of vessel edges.

Fourteen 45° 1392x1038 color fundus images acquired with Nidek MP1 were tested by the proposed method.

The disk boundary manually marked by a retinal specialist was assumed as the ground truth, and the average distance from the detected boundary point to the ground truth is measured for evaluation.

Results show a good detection of the border, with an average distance of 3.44 pixels. The highest error is caused by wrong classification of the reliable contour points, so better results could be obtained mainly by improving this step.

10.1.4 Fovea Detection

Fovea identification is a fundamental task in any study of ocular diseases, because it is the highest accuracy vision zone of the retina, so the nearer the fovea are the more serious the ocular lesions are. The geometrical relation between fovea, optic disc and blood vessels is exploited to locate the fovea. The shape of the main courses of the blood vessels is roughly a parabolic curve, with vertex inside the OD and the fovea is approximately situated about at 2 disc diameters from the optic disc along the direction of the main axis, estimated using a method based on image moments. Then two different methods are used to localize the fovea more accurately, one based on watershed transform and one based on vascular density analysis (fovea is an avascular zone). At last a linear classifier decides the more reliable method to be used for each image.

The algorithm proposed for fovea localization was tested on 80 mosaic images acquired with Orion Nidek, with a mean distance from ground truth of 260 microns (37 pixels).

Results show the importance of the classifier that chooses the most reliable method, so further developments should focus on improving the performance of this classifier.

10.1.5 Estimation of Generalized Arterioral Narrowing

A sign that have been shown to be related to cardiovascular diseases is the generalized arteriolar narrowing, usually expressed by the arteriolar to venular diameter ratio (AVR).

To overcome the long and cumbersome manual measurements we proposed a computer assisted procedure, which requires several steps: vessel tracing, ROI detection, artery-vein classification and AVR estimation with both the standard and the revised formulas

We have used as reference values, against which the automatic results were to be compared, the results of a manual AVR estimation. This latter was carried out by manually performing all steps on the retinal image displayed on a PC monitor: identification of OD and its diameter (and thus of the ROI for caliber estimation), vessel labeling as arteries or veins, vessel diameters

measurement by drawing segments with the mouse and computing their pixel length.

The automatic procedure appears to behave better with the standard formula than for the revised one as regards correlation, 0.83 vs 0.73, whereas automatic/manual ratios have identical average and standard deviations but different range.

A good correlation was found between automatic and manual AVR values when using the standard formula.

Two outliers significantly affect the overall performance. A semi-automatic procedure was then carried out, where selected steps were manually performed in order to identify the reason for the unsatisfactory performance in these images. From this investigation, it appears that vessels missed by the tracing procedure and faulty A/V discrimination are the main reasons for these unsatisfactory performances.

The revised formula provides a slightly worse correlation, but with a much more homogeneous behavior, as no outliers are evident in the scatter-plot and automatic/manual ratios exhibit a narrower range.

10.2 – Diabetic Retinopathy Screening and Grading

Some of the methods presented in this thesis have been used in an artificial intelligence camera system that screens for diabetic retinopathy (DR). The results have been presented at the AAO 2007 meeting. In this study 240 subjects were selected from the patient population of a diabetic retinopathy screening clinic at the University of Padova. Subjects included normals or diabetic subjects with no diagnosed retinal pathology and diabetic subjects with DR pathology.

After several steps of image processing, including image mosaicing, vessel segmentation and optic disc localization, 10% of the images were used to train two neural networks, one sensitive to bright pathology and another sensitive to dark pathology.

The remaining images were used to independently score the results of the trained neural networks, obtaining 96.2% of sensitivity and 98.7% in

detecting DR . In future works also fovea identification will be included in this system in order to be able to grade the severity of retinopathy.

Bibliography

[1] L. G. Brown, “A survey of image registration techniques,” *ACMComput. Surv.*, vol. 24, pp. 325–376, Dec. 1992.

[2] B. Zitova and J. Flusser, “Image registration methods: A survey,” Image Vision Comput., vol. 21, pp. 977–1000, 2003.

[3] P. A. van den Elsen, E. D. Pol, and M. A. Viergever, “Medical image matching—A review with classification,” IEEE Eng. Med. Biol. Mag., vol. 12, no. 1, pp. 26–39, Mar. 1993.

[4] J. B. A. Maintz and M. A. Viegever, “A survey of medical image registration,” in Medical Image Analysis. Oxford, U.K.: Oxford Univ. Press, 1998.

[5] G. K. Matsopoulos, N. A. Mouravliansky, K. K. Delibasis, and K. S. Nikita, “Automatic retinal image registration scheme using global optimization techniques,” IEEE Trans. Inf. Technol. Biomed., vol. 3, no. 1, pp. 47–60, Mar. 1999.

[6] N. Ritter, R. Owens, J. Cooper, R. H. Eikelboom, and P. P. V. Saarloos, “Registration of stereo and temporal images of the retina,” IEEE Trans. Med. Imag., vol. 18, no. 5, pp. 404–418, May 1999.

[7] E. De Castro and C. Morandi "Registration of Translated and Rotated Images Using Finite Fourier Transforms", IEEE Transactions on pattern analysis and machine intelligence, Sept. 1987

[8] F.Zana, J.Klein. A multimodal registration algorithm of eye fundus images using vessels detection and hough transform. IEEE Transactions on Medical Imaging, 18(5):419-428,May 1999.

[9] J.Domingo,G.Ayala,A.Simò,E.de Ves.Irregular motion recovery in fluorescin angiograms.pattern recognition letters,18:805-821,1997.

[10] C.D. Kuglin and D.C. Hines, “The phase correlation image alignment method” in Proc. 1975 Int. Conf. Cybernetics and Society, Sept.1975,pp. 163-165.

[11] A.Can, C.Stewart,B.Roysam,L.Tanenbaum.”A feature-fased,robust,hierarchical algorithm for registering pairs of images of the curved human retina.IEEE transactions on pattern analysis and machine learning,vol.24, n.3, march 2002

[12] L. D. Hubbard, R. J. Brothers, W. N. King, L. X. Clegg, R. Klein, L.S. Cooper, A. R. Sharrett, M. D. Davis, and J. Cai, “Methods for evaluation of retinal microvascular abnormalities associated with

hypertension/sclerosis in the atherosclerosis risk in communities study," Ophthalmology,vol. 106, pp. 2269–2280, Dec. 1999.

[13] M. Foracchia, E. Grisan, A. Ruggeri, Detection of optic disc in retinal images by means of a geometrical model of vessel structure, IEEE Trans. Med. Imaging 23 (10) (2004) 1189–1195.

[14] C. Sinthanayothin, J. F. Boyce, H. L. Cook, and T. H.Williamson, "Automated localisation of the optic disc, fovea and retinal blood vessels from
digital colour fundus images," British Journal of Ophtalmology, vol. 83, pp. 231–238, August 1999.

[15] S. Tamura and Y. Okamoto, "Zero-crossing interval correction in tracing eye-fundus blood vessels," Pattern Recognition, vol. 21, no. 3, pp. 227–
233, 1988.

[16] T. Walter and J.-C. Klein, "Segmentation of color fundus images of the human retina: Detection of the optic disc and the vascular tree using morphological techniques," proc. Second International Symposium on Medical Data Analysis (ISMDA 2001), pp. 282–287, October 2001.

[17] H. Li, O. Chutatape, Automatic location of optic disk in retinal images, in: Proceedings of the International Conference on Image Processing, vol. 2, October 2001, pp. 837–840.

[18] M. Lalonde, M. Beaulieu, L. Gagnon, Fast and robust optic disc detection using pyramidal decomposition and Hausdorff-based template matching, IEEE Trans. Med. Imaging 20 (11) (2001) 1193–1200.

[19] A. Osareh, M. Mirmehd, B. Thomas, R. Markham, Comparison of colour spaces for optic disc localisation in retinal images,
in: Proceedings of the 16th International Conference on Pattern Recognition, vol. 1, August 2002, pp. 743–746.

[20] J. Lowell, A. Hunter, D. Steel, A. Basu, R. Ryder, E. Fletcher, L. Kennedy, Optic nerve head segmentation, IEEE Trans. Med. Imaging 23 (2) (2004) 256–264.

[21] E.Grisan, A.Pesce, A.Giani, M.Foracchia, A.Ruggeri," A New tracking system for the robust extraction of retinal vessel structure", Proceedings of the 26th Annual International Conference of the IEEE EMBS San Francisco, CA, USA • September 1-5, 2004

[22] M.Kass,A.Witkin,D.Terzopoulos "Active contour models". International Journal of Computer Vision, pages 321-331,1988.

[23] A.Amini, S.Tehrani, and E.Weimouth, Using dynamic programming for minimizing the energy of active contours in the presence of hard constraints, in Proceedings, second International Conference on Computer Vision,1988,pp. 95-99.

[24] D.Williams, M. Shah, " A fast algorithm for active contours and curvature estimation". CVGIP:IMAGE UNDERSTANDIBG Vol.55, No.1, January, pp.14-26,1992

[25] J.Xu, O. Chutatape, E. Sung, C.Zheng, P. Chew,"Optic disk feature extraction via modified deformable model technique for glaucoma analysis" Pattern recognition 40(2007) 2063-2076

[26] M.Foracchia, E.Grisan, A.Ruggeri."Luminosity and contrast normalization in retinal images". Medical Image Analysis, Volume 9, issue 3, pages 179-190.

[27] M.Ibanez, A.Simo. "Bayesian detection of the fovea in eye fundus angiographies". Pattern Recogn.Lett.20,229-240.

[28] Sinthanayothin,C.,Boyce, J.F., Cook,H.L.,Williamso n,T.H., 1999.Automated localisation of the optic disc,fovea, and retinal blood vessels from digital colour fundus images. Br. J. Ophthalmol. 83,902–910.

[29] Goldbaum,M.,Moezzi, S.,Taylor, S.,Chatterjee ,S., Boyd, J.,Hunter,E., Jain, R., 1996. Automated diagnosis and image understanding with object extraction,object classification, and inferencing in retinal images. In: Proceedings of the IEEE International Conference on Image Processing,vol. 3. Los Alamitos,USA,pp. 695–698.

[30] H.Li, O. Chutatape." Automated feature extraction in color retinal images by a model based approach. IEEE Trans. Biomed. Eng. 51,246–254.

[31] Meyer F., beucher S., "Skeletons and perceptual graphs", Signal Process., Vol. 16, n.4,pp. 335-363, April 1989.

[32] Soille P. and Vincent L., "Determing watersheds in digital pictures via flooding simulations", Proceeding SPIE, Vol. 1360, Visual Comm. and Image Proc. '90, Oct 1990.

[33] Vincent, Luc, and Pierre Soille, "Watersheds in Digital Spaces: An Efficient Algorithm Based on Immersion Simulations," IEEE Transactions of Pattern Analysis and Machine Intelligence, Vol. 13, No. 6, June 1991, pp. 583-598.

[34] T. Y. Wong, R. Klein, B. E. K. Klein, and J. M. Tielsch et al., "Retinal microvascular abnormalities, and their relation to hypertension,

cardiovascular diseases and mortality," Survey Ophthalmol., vol. 46, pp. 59–80, 2001.

[35] L. D. Hubbard and R. J. Brothers et al., "Methods for evaluation of retinal microvascular abnormalities associated with hypertension sclerosis in the atherosclerosis risk in communities studies,"Ophthalmology, vol. 106, pp. 2269–80, 1999.

[36] T. Y. Wong, M. Knudtson, R. Klein, B. E. K. Klein, S.M. Meuer, L. D. Hubbard, "Computer-assisted measurement of retinal vessel diameters in the Beaver Dam eye study," Ophthalmology, vol. 111, pp. 1183–90, 2004.

[37] H. Li, W. Hsu, M.L. Lee, and T.Y. Wong "Automatic grading of retinal vessel caliber," IEEE Trans Biomed Eng, vol. 52, pp. 1352-5, 2005.

[38] M.D. Knudtson, K.E. Lee, L.H. Hubbard, T.Y. Wong, R. Klein, B.E.K. Klein, "Revised formulas for summarizing retinal vessel diameters," Current Eye Research, vol. 27, no. 3, pp. 143-149.

[39] E. Grisan and A. Ruggeri, "A divide et impera strategy for automatic classification of retinal vessels into arteries and veins," Proc. 25th Annual International Conference of IEEE-EMBS, pp. 890-4, IEEE,New York, 2003.

[40] M. De Luca,E. Grisan,A. Ruggeri.An automatic system for the estimation of generalized arteriolar narrowing in retinal images.
Proc. 29th Annual International Conference of IEEE-EMBS, IEEE, Lyon, 2007

[41] Tolias Y. A. Panas S. M., "A fuzzy vessel tracking algorithm for retinal images based on fuzzy clustering,"
IEEE Transactions on Medical Imaging, vol. 17, no. 2, pp. 263–273, Mar 1998.

[42] Hoover A., Kouznestova V., Goldbaum M. "Locating blood vessels in retinal images by piece-wise threshold probing of a matched filter response," IEEE Transactions on Medical Imaging,, vol. 19, no. 3, pp.
203–210, Mar 2000.

[43] Lowell J., Hunter A., Steel D., Basu A., Ryder R., Kennedy R. L. "Measurement of Retinal Vesssel
Widths From Fundus Images Based on 2-D Modelling," IEEE transactions on medical imaging, vol. 23, no. 10, pp. 1196-1204, Oct 2004.

[44] Leung H. et Al. "Relationships between Age, Blood Pressure, and Retinal Vessel Diameters in an Older

Population" Investigative Ophthalmology & Visual Science, July 2003, vol. 44, No. 7, pp. 2900-2904, Jul
2003.

[45] M. De Luca,A. Giani, E. Grisan, A. Ruggeri. Detecting false vessel recognitions in retinal fundus analysis. Proc. 28th Annual International Conference of IEEE-EMBS, pp. 4449-4452, IEEE, New York, 2006

[46] C. D. Murray, The physiological principle of minimum work. i. the vascular system and the cost of blood volume., Proceedings of the National Academy of Science 12 (1926), 207–214.

[47] A. V. Stanton, B. Wasan, A. Cerutti, S. Ford, R. Marsh, P. P. Sever, S. A. Thom, and A. D. Hughes, Vascular network changes in the retina with age and hypertension, Journal of Hypertension 13 (1995), 1724–1728.

[48] Early Treatement Diabetic Retinopathy Study Research Group, Grading diabetic retinopathy from stereoscopic fundus photographs - am extension of the modified airlie house classification., Ophthalmology 98 (1991), 786–806.

[49] N. M Keith, H. P. Wegener, and N. W. Barker, Some different types of essential hypertension: their course and prognosis, American Journal of Medicine Science 197 (1939), 336–354.

[50] H. G. Scheie, Evaluation of ophthalmoscopic changes of hypertension and arterial sclerosis, Archives of Ophthalmology 49 (1953), no. 2, 117–138.

[51] S. Chatterjee, S. Chattopahya, M. Hope-Ross, and P. L. Lip, Hypertensionand the eye: changing perspectives, Journal of Human Hypertension 16 (2002), 667–675.

[52] The Diabetic Retinopathy Study Research Group, A modification of the airlie house classification of diabetic retinopathy, Investigative Ophthalmology and Visual Science 21 (1981), 210–226.

[53] Early Treatment Diabetic Retinopathy Study Research Group, Early treatment diabetic retinopathy study design and baseline patient characteristics, Ophthalmology 98 (1991), 741–756.

[54] C. P. Wilkinosn, F. L. Ferries, R. E. Klein, P. P. Lee, C. D. Agardh, M. Davies, D. Dills, A. Kampik, R. Pararajasegaram, and J. T. Vardaguer representing the global Diabetic Retinopathy Project Group, Proposed international clinical diabetic retinopathy and diabetic macular edema disease severity scale, Ophthalmolgy 110 (2003), 1677–1612.

[55] S. J. Aldington, E. M. Kohner, S. Meuer, R. Klein, A. K. Sjølie, and Complication Study Group EURODIAB IDDM, Methodology for retinal photography of diabetic retinopathy: the EURODIAB IDDM Study Group, Diabetologia 38 (1995), no. 4, 437–444.

[56] S. Bursell, J. D. Cavallerano, A. A. Cavallerano, A. C. Clermont, D. Birkmire-Peters, L. P. Aiello, L. M. Aiello, and the Joslin Vision Network Research Team, Stereo nonmydriatic digital-video color retinal imaging compared with early treatement diabetic retinopathy study seven standard field 35-mm stereo color for determining level of diabetic retinopathy, Ophthalmology 108 (2001), no. 3, 572–585.

[57] D. Y. Lin, M. S. Blumenkranz, R. J. Brothers, D. M. Grosvenor, and for the digital diabetic screening group, The sensitivity and specificity of single-field nonmydriatic monochromatic digital fundus photography
with remote image interpretation dor diabetic retinopathy screening: a comparison with ophthalmoscopy and standardized mydriatic color photography, American Journal of Ophthalmology (2002), 204–213.

[58] P. Massin, A. Erginay, A. Ben Mehdi, E. Vicaut, G. Quentel, Z. Victor, M. Marret, P. J. Guillausseau, and A. Gaudric, Evaluation of a new non-mydriatic digital camera for detection of diabetic retinopathy, Diabetic Medicine 20 (2003), 635–641.

[59] J. A. Pugh, J. M. Jacobson, W. A. J. Van Heuven, J. A. Watters, M. R. Tuley, D. R. Lairson, R. J. Lorimor, A. S. Kapadia, and R. Velez, Screening for diabetic retinopathy. the wide angle retinal camera, Diabetes Care 16 (1993), no. 6, 889–895.

[60] H. M. Herbert, K. Jordan, and D. W. Flanagan, Is screening with digital imaging using one retinal view adquate?, Eye 17 (2003), no. 3, 497–500.

[61] ARIC, ARIC protocol 14A retinal photography, ARIC Coordinating Center, Department of Biostatistics (CSCC), University of North Carolina, August 1995.

[62] ARIC protocol 14B retinal reading protocol, ARIC Coordinating Center, Department of Biostatistics (CSCC), University of North Carolina, May 1996.

[63] G. A. Williams, I. U. Scott, J. A. Haller, A. M. Maguire, D. Marcus, and H.R. McDonald, Single-field fundus photography for diabetic retinopathy screening, Ophthalmology 111 (2004), no. 5, 1055–1012.

[64] I. Liu and Y. Sun, Recursive tracking of vascular networks in angiograms based on the detection-deletion scheme, IEEE Transactions on Medical Imaging 12 (1993), no. 2, 334–341.

Acknowledgements

I would like to express my sincere gratitude to all the people who, in different ways, supported me in this work. My special thanks go to :
Prof. Alfredo Ruggeri for having trusted in my capacities and for his research guidance.
All the researchers who worked with me on different projects at DEI, in particular Alfredo Giani and Enrico Grisan for their important advices and support in this work.
All the people who worked next to me at Nidek Technologies.

This work has been founded by Nidek Technologies